RSC Advances

PAPER

View Article Online
View Journal | View Issue

Check for updates

Cite this: *RSC Adv.*, 2025, **15**, 21006

Received 12th May 2025
Accepted 16th June 2025

DOI: 10.1039/d5ra03333k

rsc.li/rsc-advances

# Safflower plant extract as a sustainable corrosion inhibitor for carbon steel in acidic media: a combined electrochemical and computational study

Qahtan A. Yousif, *[a] Sumit Sahil Malhotra,[b] Mahmoud A. Bedair, *[c] Azaj Ansari *[b] and Ali K. Hadi[d]

This study investigates the corrosion inhibition efficiency of safflower plant (SP) extract on carbon steel in hydrochloric acid (HCl) solutions. The SP extract, obtained through Soxhlet extraction, was tested for its ability to reduce corrosion using electrochemical techniques, including potentiodynamic polarization, electrochemical impedance spectroscopy (EIS), and electrochemical frequency modulation (EFM). The study revealed that the SP extract functions as an effective mixed-type inhibitor, significantly reducing the corrosion current density and enhancing inhibition efficiency at concentrations up to 2.5 g $L^{-1}$. It achieved an inhibition efficiency of 89.56% at 2.5 g $L^{-1}$. The adsorption mechanism is described in terms of both physical and chemical adsorption processes, with the Langmuir isotherm fitting the adsorption data. Computational modeling using density functional theory (DFT) further supported the experimental findings, identifying key active compounds in SP extract that contribute to its inhibitory performance. The study demonstrates the potential of SP extract as a sustainable and eco-friendly corrosion inhibitor for industrial applications.

## 1. Introduction

The corrosion of metals is widely recognized as a significant economic phenomenon. Corrosion significantly reduces the longevity of metals, especially steel, which is widely utilized.[1,2] Using acid solutions can significantly damage enterprises due to the substantial costs associated with corrosion-related maintenance and production losses.[3,4] Halting corrosive reactions lowers the economy's growing need for natural resources and the amount of hazardous materials created and released into the environment.[5,6] The chemical composition of these compounds will impact the corrosion process.[7,8] Reactive and unstable metals engage in electrochemical processes in their surroundings, creating more stable elements and reducing energy.[9,10] Carbon steel is crucial in numerous industries, emphasizing its significance in the oil and gas sector.[11,12] Carbon steel is the most extensively utilized engineering material globally, contributing to an estimated 85 percent of annual steel production.[13,14] Carbon steel corrosion poses a significant challenge for numerous industries, especially in the oil and gas sector.[15,16] Its detrimental effects extend beyond production stability and can have a detrimental impact on project economics.[5,17] Studies of carbon steel corrosion in acidic media, particularly hydrochloric acid, have become more critical since acid solutions are widely used in industry.[18,19] The corrosion of metallic objects in an acidic solution is quite expensive.[20,21] In the past, industrial corrosion inhibitors included inorganic salts and organic substances. However, these inhibitors were ineffective at delaying corrosion because they were expensive and dangerous and posed health and environmental dangers in the event of a severe loss in output.[22–24] Thus, most conventional organic and inorganic corrosion inhibitors are hazardous and can cause environmental problems when disposed of.[25] Regulations related to the environment further limit their applicability.[26] For example, environmental pollution occurs when oilfield inhibitors are released from offshore production platforms into the ocean, endangering marine life.[27] Green or ecologically friendly corrosion inhibitors prepared from natural materials have emerged. Since 1960, plant extracts have been used to prevent corrosion in an environmentally sustainable manner.[17,28] The first plant extract used for this purpose was tannin.[29] There are many different plant parts and components from which extracts can be prepared.[30] Many chemical structures, such as aromatic rings, carbonyl, carboxylic, amine, and hydroxyl, can be found

---

[a] *Department of Materials Engineering, College of Engineering, University of Al-Qadisiyah, Iraq. E-mail: qahtan.adnan@qu.edu.iq*
[b] *Department of Chemistry, School of Basic Sciences, Central University of Haryana, Mahendergarh, 123031, Haryana, India. E-mail: ajaz.alam2@gmail.com*
[c] *Department of Chemistry, College of Science, University of Bisha, P.O. Box 511, Bisha, 61922, Saudi Arabia. E-mail: mbedair@ub.edu.sa; m_bedier@yahoo.com*
[d] *College of Health and Medical Technologies, University of Al-Kafeel, Iraq*

in these natural sources.[31,32] These substances work as efficient inhibitors to retard the corrosion of metals and alloys, particularly in acidic environments.[33] Because so many plant resources are available, these plant extracts are also widely accessible.[34] However, alternatives are more eco-friendly and derived from plants, which can be used instead of synthetic corrosion inhibitors.[35,36] Several researchers have come up with hypotheses to try to explain this phenomenon since the way green corrosion inhibitors work depends on the structure of the active ingredient.[37–41] Thus, plant extracts' inhibitory mechanism is often based on their physical or chemical adsorption on the metal surface, which creates a barrier that prevents the corrosive species from accessing the metal and slows down metal breakdown.[17,30] An examination of research on developing plant inhibitors for carbon steel indicates that these studies have predominantly concentrated on carbon steel in HCl environments.[42,43] This is because carbon steel is extensively used in various applications, such as chemical and electrochemical processes like acid pickling, cleaning, and etching, which require using acidic solutions, particularly HCl.[44,45] Numerous organic compounds, including flavonoids, alkaloids, phenols, and tannins, found in plant extracts have demonstrated corrosion-inhibitive properties.[46] The plant extracts contain phenolic compounds that effectively adsorb on the metal surface and impede corrosion.[47] Various extraction methods, such as Soxhlet extraction and ultrasound-assisted extraction, can obtain extracts from different plant parts, such as seeds, stems, pulp, and leaves, altering the significant constituents and their anticorrosive activity.[48] Many studies have used plant extracts as corrosion inhibitors for various metals and alloys under different corrosive conditions.[17,49,50] Only Fouda and his group, as well as Nasibi and his group, have conducted any recent studies on using the safflower plant (SP) as a corrosion inhibitor.[51,52] Both studies used an infusion of the plant's leaves as an inhibitor to investigate the corrosion effect on commercial 60/40-brass samples and mild steel, respectively. This research used the Soxhlet method to investigate how SP extract, a cheap and naturally occurring substance, inhibits carbon steel corrosion in HCl acid solutions using electrochemical and surface analysis methods. Density functional theory (DFT) helps us understand the electrical properties of molecules that stick to surfaces at the molecular and atomic levels. This lets us study how well plant extracts stop corrosion and how they work, as well as learn more about how chemicals react and work to prevent corrosion.

## 2. The experimental methods

### 2.1. SP extract preparation

Since antiquity, safflower flowers (Fig. 1) have been cultivated for their use in fabric dyeing, culinary coloring, and seasoning applications. The terminology "Safflower" is derived from its substantial contribution to the dyeing sector. The seeds' oil produces illumination, paint, and varnish.

The desiccated safflower flower samples were procured from a local vendor, pulverized into a powder using a blender and processed through pure water extraction. The powder (2.0 g) of crushed leaves was extracted twice at 95 °C using Soxhlet extraction in deionized water (1000 mL). The acquired solution was subsequently concentrated at −0.05 MPa and desiccated at 80 °C. SP has been used at concentrations between 0.5 and 2.5 g $L^{-1}$. Because it is hygroscopic, the extract must be stored dry and cold in a small, tightly sealed container. The largest and most significant constituents of the SP extract were identified by

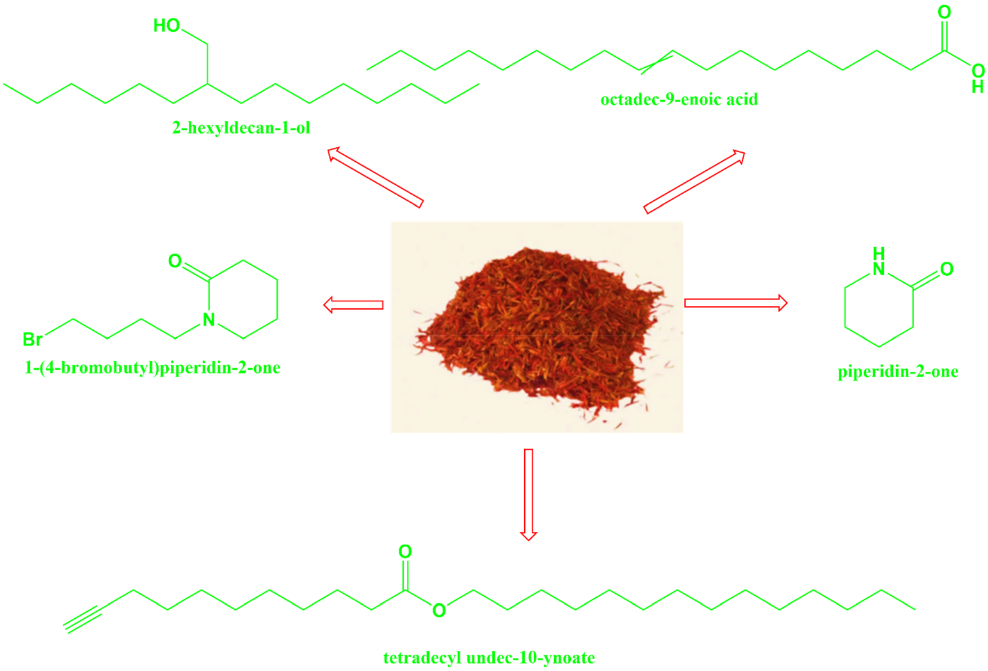

Fig. 1 Leaves of safflower flowers and the chemical structure of some important molecules present in it.

GS/mass (Shimadzu Instruments), and the chemical results showed that the safflower concentrate contains 2-piperidinone, *N*-[4-bromo-*n*-butyl], 2-hexyl-1-decanol, 2-piperidone, 9-octadecenoic acid, undec-10-yonic acid, and tetradecyl ester.

### 2.2. Material preparation

Commercially available materials were used without any additional purification. The acid solutions were prepared by diluting 37% hydrochloric acid (Sigma-Aldrich) with distilled water. Each experiment utilized 150 mL of electrolyte. The working electrode consisted of carbon steel specimens with a nominal composition of 2.19% C, 1.36% Mn, 3.10% Si, 0.10% Cr, 0.12% Mo, 0.21% Ni, and 0.59% Cu, and the remaining balance was Fe. The coupons were trimmed to dimensions of 1.5 × 1.5 cm and then coated with polyester resin, resulting in a final surface area of 1 $cm^2$. The carbon steel substrates were manually abraded using several grades of emery paper, ranging from rough to smooth, to achieve an appropriate soft primary surface. Subsequently, the substrates were degreased using acetone and benzene solvents and rinsed with distilled water before each electrochemical experiment. A 0.5 N hydrochloric acid (HCl) solution was prepared by diluting 37% HCl with distilled water. Each experiment utilized 150 mL of the electrolyte.

### 2.3. Electrochemical measurement and surface inspection

A typical three-electrode cell configuration was used for the electrochemical testing, with carbon steel as the working electrode, platinum as the counter electrode, and a saturated calomel electrode (SCE) as the reference electrode. Before measurements, the working electrode (carbon steel) was immersed in the test solution (0.5 M HCl ± SP extract) for 30 min to achieve a stable $E_{\text{ocp}}$. The potentiostat device was employed to study polarization at a 3 mV $s^{-1}$ scan rate. Eqn (1) was used to calculate the inhibitory efficiency[53] ($\eta_{\text{P}}$).

$$\eta_{\text{P}}\ \% = 100\left(1 - \frac{i_{\text{corr}}}{i^0_{\text{corr}}}\right) \tag{1}$$

The corrosion current densities are denoted as $i^0_{\text{corr}}$ and $i_{\text{corr}}$, correspondingly, in the absence and presence of different inhibitor concentrations. The EIS tests were conducted potentiostatically at the open-circuit potential ($E_{\text{ocp}}$) to avoid polarization effects and ensure a stable interface. A frequency response field of 1 Hz to 100 kHz was used for the impedance test, with amplitude of ±10 mV. Applying an appropriate equivalent circuit to fit the impedance data allows for extracting all the information from the EIS. Estimating charging transfer resistance ($R_{\text{ct}}$), solution resistance ($R_{\text{s}}$), and inhibition efficiency ($\eta_{\text{E}}$ %). The impedance spectrum was shown *via* Nyquist and Bode graphs. The corrosion inhibition efficiency ($\eta_{\text{E}}$ %) was determined using eqn (2) (ref. 54) based on the available data. The charge transfer resistances $R_{\text{ct}}$ and $R^0_{\text{ct}}$ represent the inhibitor's presence and absence, respectively.

$$\eta_{\text{E}}\ \% = 100\left(\frac{R_{\text{ct}} - R^0_{\text{ct}}}{R_{\text{ct}}}\right) \tag{2}$$

In addition, to fulfill the requirements of electrochemical frequency modulation (EFM), a potential perturbation signal with amplitude of 10 millivolts and two sine waves with frequencies of 2 and 5 hertz together with 16 cycles are also utilized. The more prominent peaks were utilized to calculate the corrosion current density ($i_{\text{corr}}$), Tafel slopes ($\beta_{\text{c}}$ and $\beta_{\text{a}}$), and causality factors (CF-2 and CF-3). Eqn (3) can be utilized to find out the degree of efficiency.[55]

$$\eta_{\text{F}}\ \% = 100\left(1 - \frac{i_{\text{corr}}}{i^0_{\text{corr}}}\right) \tag{3}$$

To investigate the alterations in surface morphology, the electrodes were exposed to an SP inhibitor; the specimens were immersed in a solution of 0.5 N hydrochloric acid containing 2.5 g $L^{-1}$ safflower extract at 25 °C. After 72 hours of waiting, the electrodes were removed from the solution, washed with distilled water, and dried. Then, images were taken using a Sigma 300 machine set to energy-dispersive X-ray analysis (EDX) for field emission scanning electron microscopy (FE-SEM). The FE-SEM profile details are recorded as resolution: 1 kV (2.2 nm), maximum scan speed (ions/pixel), accelerating voltage: 0.02–30 kV.

### 2.4. Computational analysis techniques

We modelled the compounds **1** to **5** (compound **1**: 2-hexyldecan-1-ol, compound **2**: octadec-9-enoic acid, compound **3**: 1-(4-bromobutyl)piperidin-2-one, compound **4**: piperidin-2-one and compound **5**: tetradecyl undec-10-ynoate) with the help of Gauss view 6.1 (ref. 56) software and performed geometry optimizations by using Gaussian 16.[57] In this current research work, B3LYP[58,59] functional and 6-311G (d,p)[60] basis set is employed for all the optimizations. The density of states (DOS) is calculated by using GaussSum software.[61] Hydrogens are omitted for the better clarification of pictures.

## 3. Results and discussion

### 3.1. Electrochemical assessments

**3.1.1 Open-circuit potential (OCP) curves.** The OCP is a straightforward electrochemical technique that offers initial insights into the processes at the interface between the metal and electrolyte. It represents the potential disparity between the working electrode and the standard or reference electrode without any external current. Before doing the electrochemical experiments, it is necessary to establish a steady state.[62] For this reason, establishing a stable OCP is crucial before doing potentiodynamic polarization, electrochemical impedance spectroscopy, and electrochemical frequency modulation experiments. As part of the experimental procedure, the working carbon steel electrode is immersed in the test solution before each concentration gradient test. Fig. 2 depicts the variations in open circuit potential over 900 seconds after being immersed for one hour. The OCP *vs.* time curves for the inhibited and uninhibited circumstances display nearly linear trends, suggesting establishing a stable potential in both

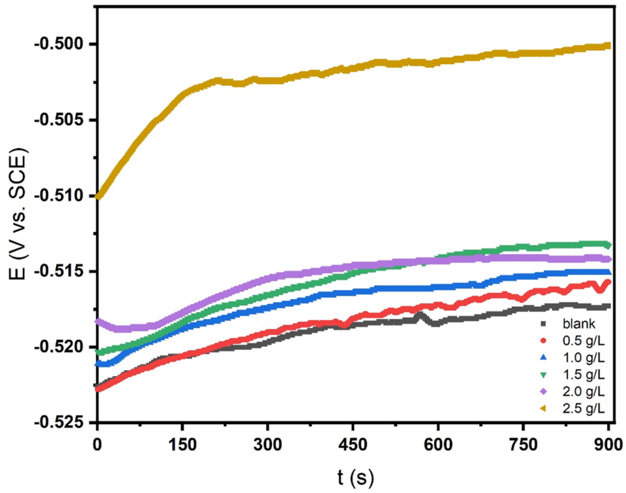

Fig. 2 OCP *vs.* time curves for steel in 0.5 N HCl solution without and with different concentrations of SP at 25 °C.

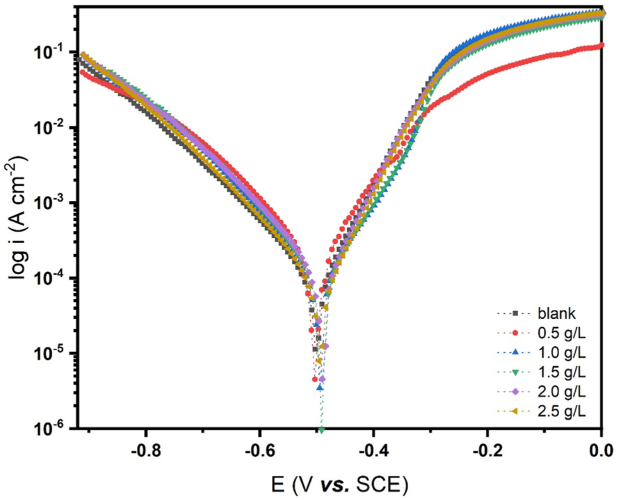

Fig. 3 Potetiodynamic polarization curves for steel in 0.5 N HCl solution without and with different concentrations of SP at 25 °C.

possibilities. Based on the measurements, the OCP value in a blank solution becomes stable at a less negative value, specifically −0.522 V. This occurs due to the dissolution of carbon steel in a 0.5 N HCl acidic medium and the accumulation of corrosion products on the metal's surface. Put another way, the steady state is reached in a blank solution by introducing the possibility of a tiny shift to the positive side. Adding varying concentrations of SP extract into a 0.5 N HCl solution shifts the OCP values in a positive direction. This shift occurs because of the separation of charges at the interface between carbon steel and the SP/solution.

Similar behavior is shown in the literature.[63,64] Positive shifts in OCP values suggest the formation of a protective coating on the surface of carbon steel, which reduces its dissolution. This phenomenon can be attributed to the adsorption of SP extracts onto the surface of the carbon steel. Fig. 2 demonstrates that the OCP value of the blank solution differs only slightly (maximum of 0.012 V) from the OCP values of the different concentrations of SP in a 0.5 N HCl solution. This shows that SP can be categorized as a mixed-type corrosion inhibitor. In a highly acidic environment, the anodic process involves the transfer of metal ions into the solution. In contrast, the cathodic process reduces hydrogen ions to generate hydrogen gas.[65] SP is classified as a mixed-type corrosion inhibitor, which can influence both the anodic and cathodic processes.

**3.1.2 Potentiodynamic (PD) measurements.** Plotting polarization curves is a relatively new technique compared to more conventional approaches, such as the gravimetric method. One of the most significant benefits of this method is that it allows for the rapid estimation of the corrosion rate based on the densities of corrosion currents. As shown in Fig. 3, the carbon steel electrode's representative PD curves were obtained in a 0.5 N HCl solution with and without different concentrations of SP inhibitor.

As indicated in Table 1, the following electro-chemical and kinetics parameters can be calculated by extrapolating Tafel polarization curves: corrosion potential ($E_{\mathrm{corr}}$), corrosion current density ($i_{\mathrm{corr}}$), anodic Tafel slope ($\beta_a$), cathodic Tafel slope ($\beta_c$), coverage area ($\theta$), and inhibition efficiency ($\eta_P$). The Tafel plots reveal that adding the inhibitor shifts the polarization curves towards less negative potentials, aligning with the OCP method's results. Similarly, we found that the corrosion current density decreased as the concentration of the SP inhibitor in the 0.5 N HCl acid solution increased, leading to a rise in the effectiveness of inhibition. The addition of various concentrations of SP inhibitor in this investigation moderately influences the values of $\beta_a$ and $\beta_c$. This demonstrates that the SP inhibitor alters the corrosion reaction and controls both the cathodic and anodic reactions. The lowest $i_{\mathrm{corr}}$ value (213.6 μA for Blank, 22.28 μA for SP extract 2.5 g L$^{-1}$) was recorded at the highest inhibitor concentration. The inhibitory efficiency increases at 2.5 g L$^{-1}$ concentration ($\eta_P$ % = 89.56%). Previous studies[23,24,66] have elucidated these findings, demonstrating that the decrease in $i_{\mathrm{corr}}$ results from the adsorption of SP extract molecules onto the metal surface and the creation of films on the active sites. This film formation reduces the medium's corrosive nature at the carbon steel and acid solution interface. Table 1 establishes a direct correlation between the corrosion current density and the corrosion rate. The carbon steel's surface coverage increases as SP concentration increases. A protective layer formed by more inhibitor molecules adsorbing to the surface lowers the corrosive current. Thus, the $E_{\mathrm{corr}}$ values change slightly when an SP inhibitor is present, as shown in Table 1. As stated in the OCP evaluation, a maximum deviation of 09 mV was observed between the blank solution's $E_{\mathrm{corr}}$ value and the $E_{\mathrm{corr}}$ values of the different SP concentrations in a 0.5 N HCl solution (this value does not exceed 85 mV). Because of this, we say that this inhibitor is mixed.[67] The mixed-type behavior of SP extract can be attributed to its ability to adsorb onto both the anodic and cathodic sites of the carbon steel surface through nitrogen- and oxygen-containing functional groups present in the extract. These functional groups, such as –OH, –NH, and C═O (as confirmed by ATR-FTIR analysis), interact with the

Table 1 Electrochemical parameters for steel dissolution in 0.5 N HCl solution containing different concentrations of the SP extract obtained from polarization measurements at 25 °C

| Conc. (g $L^{-1}$) | $E_{corr}$ *vs.* SCE (mV) | $i_{corr}$ (μA $cm^{-2}$) | $\beta_a$ (mV $dec^{-1}$) | $\beta_c$ (mV $dec^{-1}$) | $k$ (mpy) | $\theta$ | $\eta_p$ % |
|---|---|---|---|---|---|---|---|
| — | −500 | 213.6 | 83.60 | −127.7 | 196.2 | — | — |
| 0.5 | −503 | 87.64 | 73.10 | −86.20 | 107.4 | 0.5897 | 58.97 |
| 1.0 | −496 | 76.55 | 87.50 | −101.0 | 97.15 | 0.6416 | 64.16 |
| 1.5 | −492 | 54.23 | 80.80 | −96.30 | 85.46 | 0.7461 | 74.61 |
| 2.0 | −496 | 36.45 | 77.80 | −108.7 | 78.35 | 0.8293 | 82.93 |
| 2.5 | −491 | 22.28 | 66.40 | −92.50 | 46.27 | 0.8956 | 89.56 |

metal surface *via* donor–acceptor mechanisms, thereby reducing both the dissolution of iron and the evolution of hydrogen gas.[68] The SP extract adsorbs onto the active sites of carbon steel, thereby inhibiting both anodic oxidation and cathodic reduction reactions,[69] which explains SP's inhibitory characteristics.

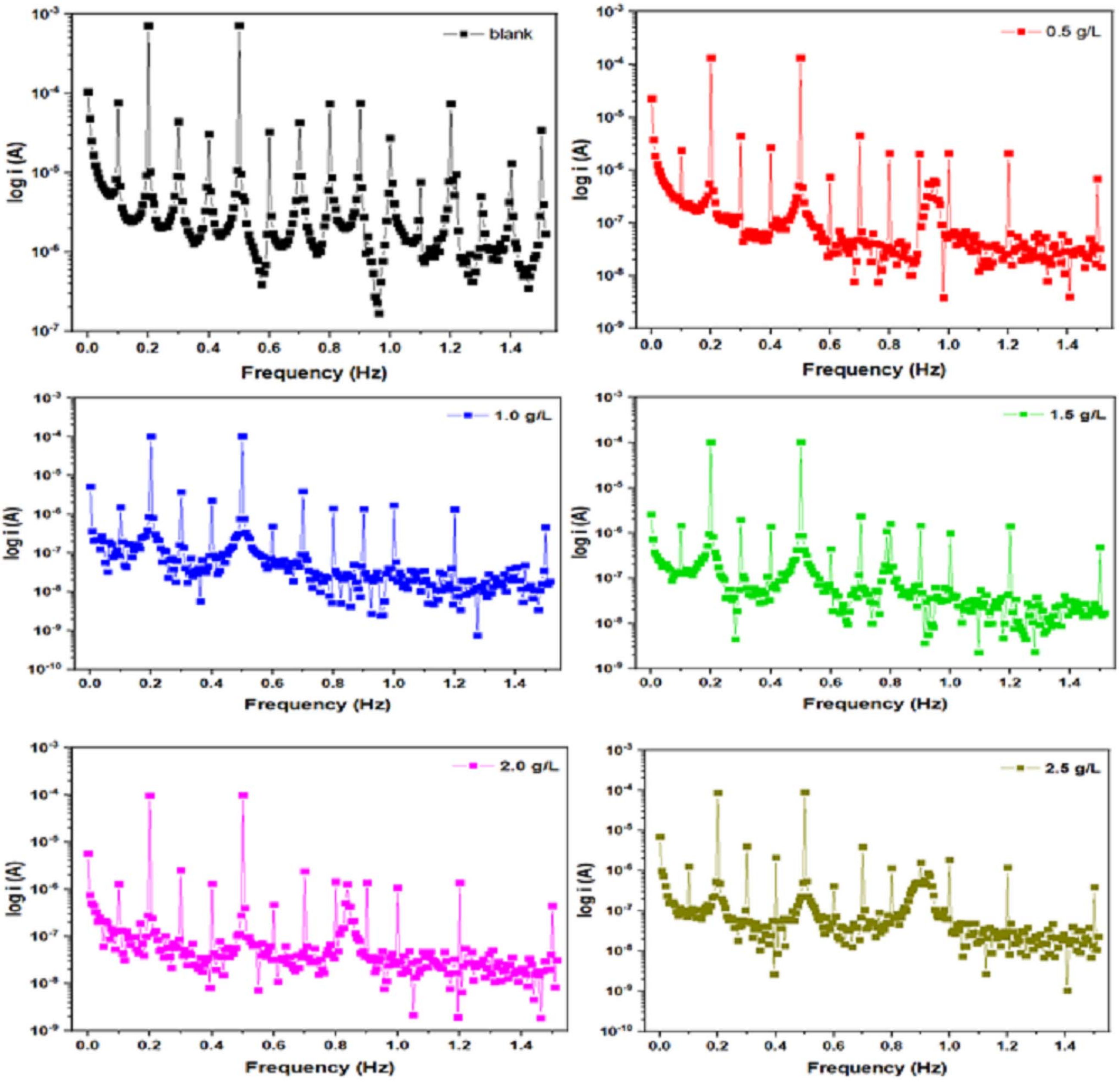

Fig. 4 Electrochemical frequency modulation curves for steel in 0.5 N HCl solution without and with different concentrations of SP at 25 °C.

Table 2 Electrochemical kinetic parameters obtained by EFM technique for steel in the absence and presence of various concentrations of SP extract in 0.5 N HCl at 25 °C

| Conc. (g $L^{-1}$) | $i_{corr}$ (μA $cm^{-2}$) | $\beta_a$ (mV $dec^{-1}$) | $\beta_c$ (mV $dec^{-1}$) | CF-2 | CF-3 | $k$ (mpy) | $\theta$ | $\eta_E$ % |
|---|---|---|---|---|---|---|---|---|
| — | 398.8 | 33 | −38 | 1.499 | 2.225 | 234.0 | — | — |
| 0.5 | 193.2 | 84 | −102 | 1.899 | 3.023 | 89.57 | 0.5155 | 51.55 |
| 1.0 | 148.7 | 89 | −112 | 1.930 | 2.998 | 69.56 | 0.6271 | 62.71 |
| 1.5 | 121.9 | 90 | −103 | 1.831 | 3.192 | 52.01 | 0.6943 | 69.43 |
| 2.0 | 96.11 | 91 | −105 | 2.059 | 3.006 | 30.14 | 0.7590 | 75.90 |
| 2.5 | 63.50 | 86 | −113 | 2.003 | 3.190 | 23.88 | 0.8407 | 84.07 |

### 3.1.3 Electrochemical frequency modulation (EFM).

EFM is an efficient and reliable method for measuring corrosion. It provides accurate values of the corrosion current without the need for Tafel constants.[70] This phenomenon occurs because of the current's non-linear potential, which causes the system to respond non-linearly to potential stimulation.[44] The frequency component of the flow response includes the input frequency, the difference, the increase, and multiple input frequency gains.[55] Electrochemical frequency modulation (EFM) can measure the gradient ($\beta_1$ and $\beta_2$), the rate of corrosion ($k$), the current density ($i_{corr}$), and the causality factors (CF-2 and CF-3) in a single set of data. Fig. 4 illustrates an example of the

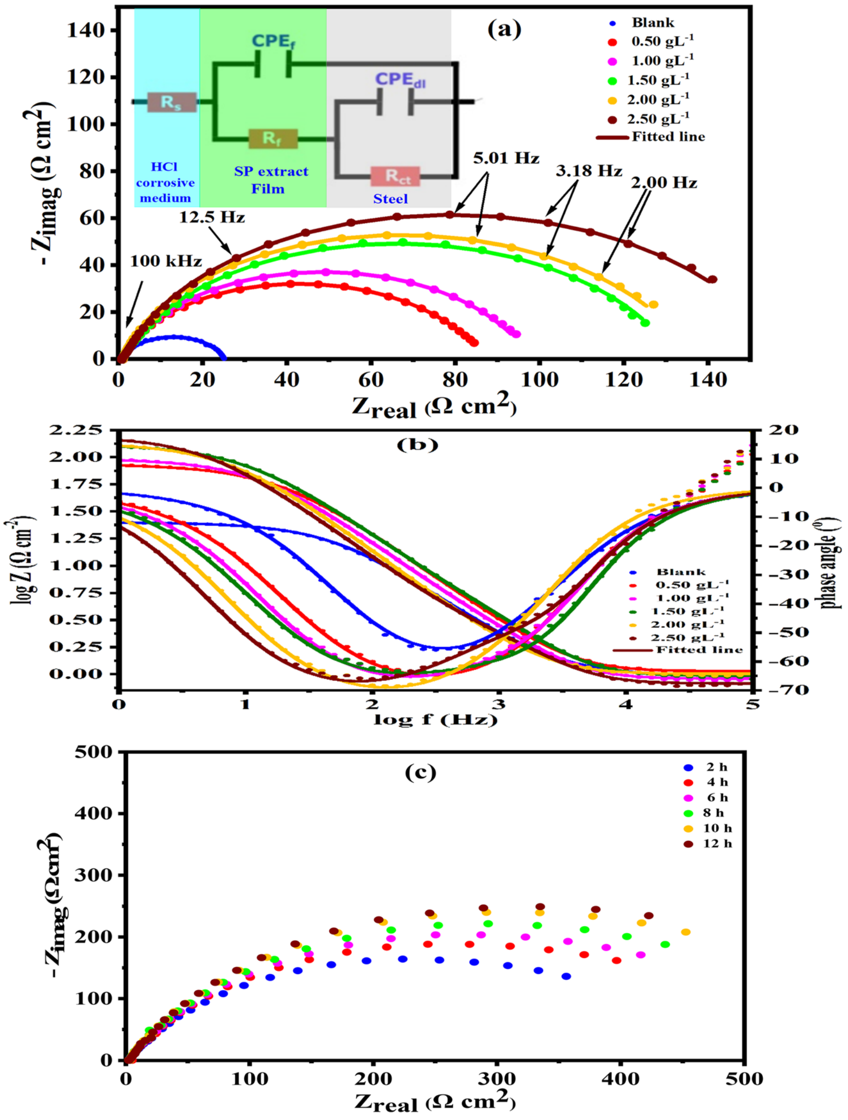

Fig. 5 Nyquist plots (a), Bode, phase angle plots (b), Nyquist plots at different immersion time (c) for steel in 0.5 N HCl solution without and with different concentrations of SP at 25 °C.

intermodulation spectrum, the EFM spectrum of SP extract. Table 2 displays the EFM electrochemical parameters for a carbon steel sample in 0.5 N HCl at 25 °C with different corrosion-inhibitory concentrations of SP extract.

Increasing the SP inhibitor's concentration decreases $i_{corr}$ while simultaneously expanding the inhibitor's effectiveness. The SP extract inhibitor was successful since the rate of corrosion dropped from 234.0 mpy to 46.88 mpy. Given that the usual values for CF-2 and CF-3 are 2.0 and 3.0, respectively,[71] any discrepancies in the causality factor values from the theoretical benchmarks may be attributed to a little perturbation amplitude, insufficient spectral frequency resolution, or a malfunctioning inhibitor. If the causative factors closely align with the expected values, a causal link exists between the perturbation signal and the response signal. The statistics are thereafter regarded as reliable. Table 2 shows casualty factor values that are becoming close to the standard values, which means the data are promising and support both the Tafel slopes and the $i_{corr}$. As mentioned earlier, applying eqn (3) yielded the inhibitory efficiency ($\eta_F$ %). SP has the highest inhibition efficiency, at 84.07%, based on the obtained percentage of efficiencies.

**3.1.4 Electrochemical impedance spectroscopy (EIS).** Electrochemical impedance spectroscopy (EIS) was used to evaluate the protective efficacy of safflower extract (SP). Fig. 5a and b illustrate the Nyquist and Bode plots for steel submerged in a 0.5 N HCl solution at 298 K. Fig. 5 depicts the impact of different concentrations of the inhibitor in a 0.5 N HCl solution. The SP did not modify the capacitance loop structure of the carbon steel relative to the uninhibited solution, suggesting that the SP molecules stuck to the steel surface, creating a protective coating.[72] The Nyquist plot shows a depressed semicircle, indicative of the double layer capacitance and its polarization resistance, which is crucial for corrosion mitigation.

The Bode plots indicate that with an increase in SP concentration, the peak magnitude also elevates, implying a decrease in the capacitive behavior of steel attributed to SP adsorption on the steel surface.[73]

An equivalent circuit model (Fig. 5a) was used to analyze the EIS data, with the findings described in Table 3. $R_s$, $R_{ct}$, and $R_f$ denote the resistances linked to the solution at the interface of the working/reference electrodes, the charge transfer mechanism, and the surface layer, respectively. In this context, the total resistance is represented by polarization resistance ($R_p = R_{ct} + R_f$). Constant phase elements (CPE) denote the capacitance of the double layer (CPEdl) and the surface film (CPE$_f$), with their values indicating the system's non-ideal characteristics.[74,75] The value 'n' measures the divergence from optimal capacitance, affected by the porous configuration of the metal surface. The chi-squared value ($\chi^2$), which is less than $10^{-2}$, indicates a robust concordance between the experimental data and the model.[76] The $R_p$ values showed a distinct correlation with differing SP concentrations, indicating improved protective efficacy with greater dose. EIS measurements were also conducted by immersing a carbon steel electrode in a 0.5 M HCl solution containing 2.5 g per L SP extract for varying durations (2–12 hours). The results are presented in Fig. 5(c). The Nyquist

Table 3 EIS parameters for corrosion of steel in 0.5 N HCl in the absence and presence of different concentrations of SP extract at 25 °C

| | | | | CPE$_f$ | | | | CPE$_{dl}$ | | | | | | | |
|---|---|---|---|---|---|---|---|---|---|---|---|---|---|---|---|
| Inhibitor | Conc. (g L$^{-1}$) | $R_s$ (Ω cm$^2$) | $R_f$ (Ω cm$^2$) | $Y_{o_1}$ (m Ω$^{-1}$ s$^n$ cm$^{-2}$) | $n_1$ | $C_f$ (μF cm$^{-2}$) | $R_{ct}$ (Ω cm$^2$) | $Y_{o_2}$ (μ Ω$^{-1}$ s$^n$ cm$^{-2}$) | $n_2$ | $C_{dl}$ (μF cm$^{-2}$) | Chi squared ($\chi^2$) | α° | $R_p$ ($R_f + R_{ct}$) | θ | $\eta_z$ % |
| Blank | 0.00 | 0.9527 | — | — | — | — | 24.09 | 318.60 | 0.8434 | 128.99 | $3.11 \times 10^{-3}$ | −55.92 | 24.09 | — | — |
| SP | 0.50 | 1.067 | 4.983 | 71.78 | 0.99975 | 71.64 | 81.31 | 316.00 | 0.7007 | 66.14 | $3.40 \times 10^{-3}$ | −64.46 | 86.29 | 0.7208 | 72.08 |
| | 1.00 | 0.9098 | 7.987 | 57.11 | 0.99896 | 56.65 | 89.02 | 292.10 | 0.7457 | 84.14 | $5.08 \times 10^{-3}$ | −64.73 | 97.01 | 0.7517 | 75.17 |
| | 1.50 | 0.967 | 13.819 | 53.39 | 0.99988 | 53.34 | 117.9 | 287.70 | 0.7462 | 91.01 | $3.93 \times 10^{-3}$ | −63.54 | 131.72 | 0.8171 | 81.71 |
| | 2.00 | 1.008 | 16.403 | 45.86 | 0.99987 | 45.82 | 119.5 | 261.80 | 0.7395 | 77.26 | $5.92 \times 10^{-3}$ | −68.52 | 135.90 | 0.8227 | 82.27 |
| | 2.50 | 0.8207 | 19.134 | 41.83 | 0.99887 | 41.49 | 137.8 | 230.60 | 0.7985 | 96.58 | $8.10 \times 10^{-3}$ | −66.03 | 156.93 | 0.8465 | 84.65 |

plot displays a capacitive reactance semicircle that increases in radius with longer immersion while maintaining its shape. This suggests that SP's inhibition efficiency strengthens over time without altering its inhibition mechanism. The slight variation in arc radius across immersion periods further supports the long-term protective effect of SP.

The inhibition effectiveness increased with greater concentrations of SP, reaching a maximum of 84.65% at 2.5 g $L^{-1}$, demonstrating its effective corrosion inhibition capability. Moreover, the $CPE_{dl}$ value decreased with the increasing SP concentration, attributable to the substitution of water molecules at the metal/solution interface by SP molecules.[77,78] This resulted in the effective protection of the steel surface from corrosion in 0.5 N HCl solution *via* the development of a protective extract layer. Table 3 illustrates a clear association between elevated SP concentrations and augmented charge transfer resistance ($R_{ct}$), resulting in enhanced inhibitory efficiency.

### 3.2. Effects of temperature and thermodynamic considerations

Inhibitor applications in corrosive systems are significantly restricted by their diminished efficacy as temperatures fluctuate, which validates the effectiveness of the SP extract inhibitor as temperatures rise. To achieve this, it is crucial to recognize that the impact of temperature on the inhibited acid–metal reaction is intricate.[79] This is because the metal surface undergoes numerous modifications, including the rapid etching and desorption of the inhibitor, as well as the

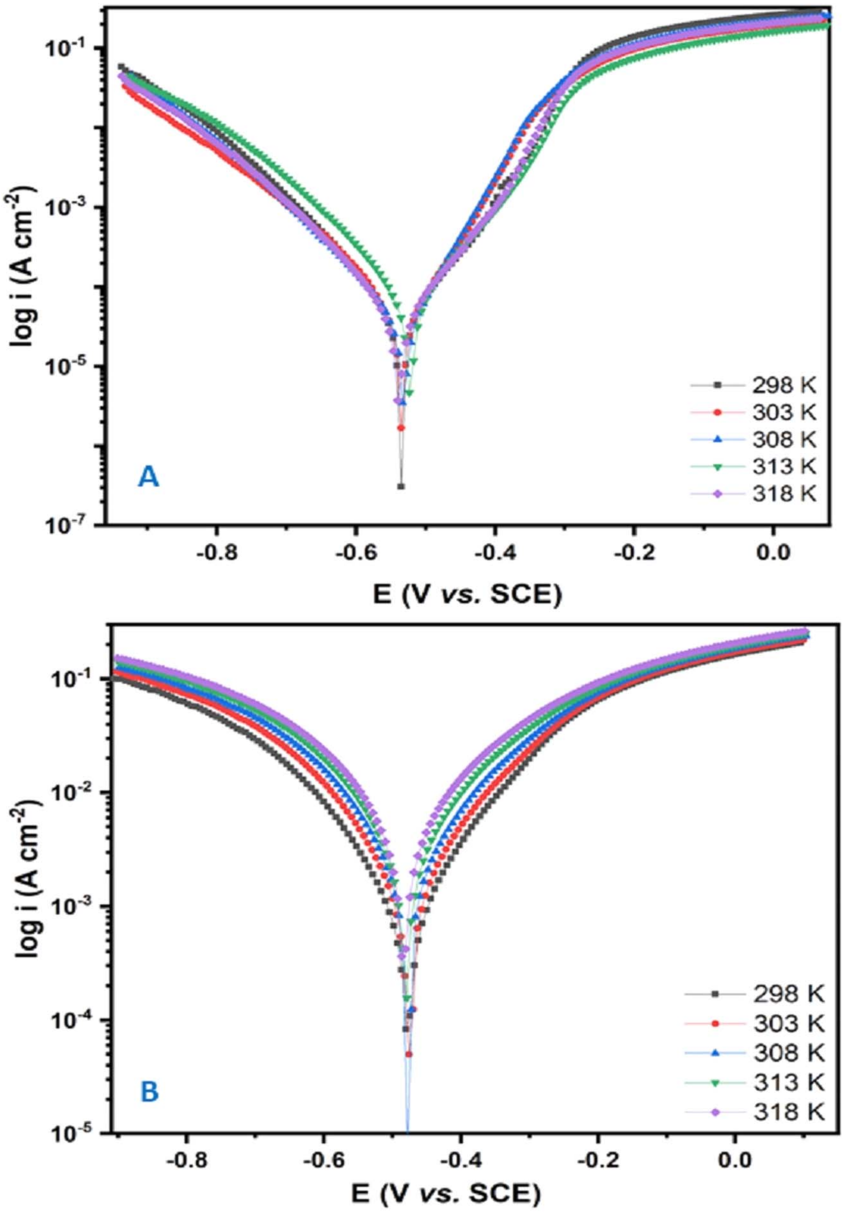

Fig. 6 Potentiodynamic polarization curves for carbon steel in a 0.5 N HCl acidic solution and an SP extract inhibitor at different temperatures.

inhibitor's decomposition and rearrangement in certain instances. Nevertheless, it provides the capacity to calculate numerous thermodynamic functions and kinetic considerations for the adsorption and inhibition processes, which are instrumental in determining the type of adsorption inhibitor. An experiment was conducted to investigate the effect of temperature on the dissolution of steel in a controlled environment. Experiments were carried out at different temperatures (298–318 K) to study the behavior of a carbon steel electrode in a 0.5 N HCl acidic solution. Additionally, specific concentrations of SP extract inhibitor were added to determine its effectiveness as a corrosion inhibitor at elevated temperatures and to understand the nature of its adsorption. Based on the analysis of these data, it is possible to infer the occurrence of either adsorption (chemisorption) or physisorption.[80] As the temperature increases, the strength of chemisorption is enhanced, while physical adsorption becomes more prominent at lower temperatures.

The polarization curves for carbon steel in a 0.5 N HCl acidic solution and an SP extract inhibitor at different temperatures can be seen in Fig. 6. Based on the data provided, the cathodic and anodic branches show increased current density with rising temperature, indicating enhanced electrochemical activity. Variations in temperature significantly affect the Tafel slopes obtained from polarization measurements. As the temperature rises, the values of corrosion potential tend to increase but eventually reach a point where they stabilize and no longer change.

Fig. 7 illustrates the relationship between the absolute solution temperature (K), the corrosive current density, and corrosion efficiency in the corrosion medium. From Fig. 7, it was clear that as the temperature rises, so does the corrosive current density of the carbon steel electrode in a solution that does not have the SP extract inhibitor. The reason for this is that as the temperature of the solution rises, reactive species move more quickly to the electrode surface and along all other corrosion pathways, including electrochemical and chemical reactions. Compared to the uninhibited system, the corrosion current densities of the inhibited systems are consistently lower. In the present study, these results suggest that the temperature range under investigation is appropriate for the SP inhibitor. Fig. 7 shows how the investigated SP inhibitor

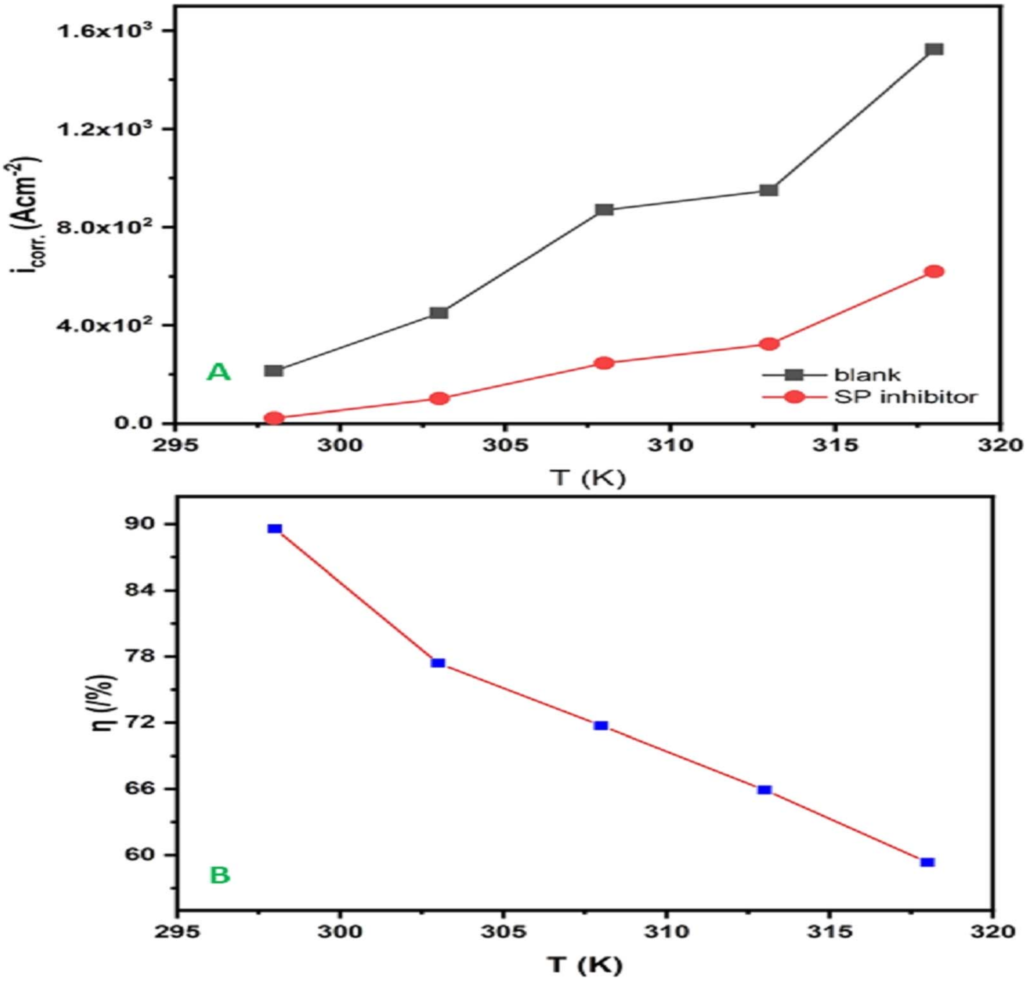

Fig. 7 The relationship between the absolute solution temperature (K), the corrosive current density (A), and corrosion efficiency in the corrosion medium (B).

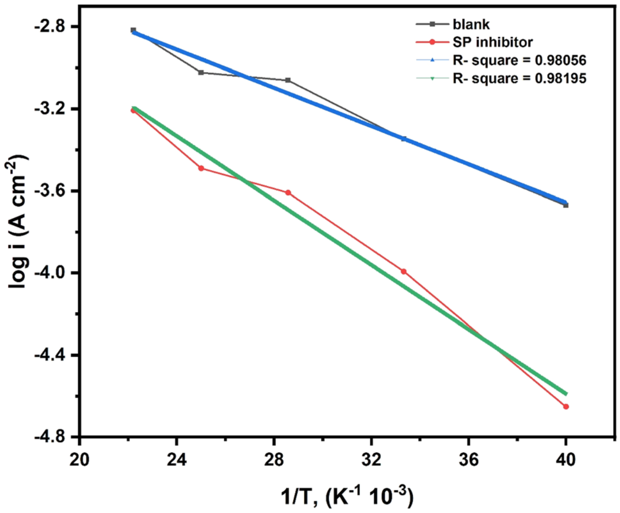

Fig. 8 The Arrhenius plot for carbon steel deterioration in the absence and presence of SP extract.

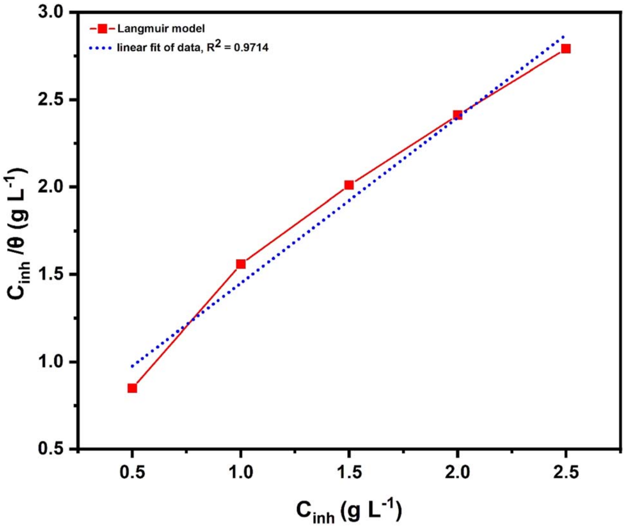

Fig. 9 Langmuir adsorption models for SP on the steel surface in 0.5 N HCl.

changed the $\eta_p$ % of carbon steel in a 0.5 N HCl acidic solution when the temperature was changed. According to this graph, the ability to provide protection decreases as the temperature of the solution increases. The performance is characterized by chemical adsorption. The reason for this is that increasing the reaction temperature reduces the strength of the bond between the inhibitor species and the metal interface. The formation and alteration of a coordinate bond result from the transfer of the π-density of molecular electrons from inhibitor molecules to open d-orbitals[81] at the electrode surface. This process forms the foundation of the chemisorption mechanism. Fig. 8 shows the Arrhenius plot for carbon steel deterioration in the absence and presence of SP extract. The following equation, based on the Arrhenius model,[82] connects the apparent activation energy ($E_a$) and the ($i_{corr}$) SP inhibitor:

$$\log i_{corr} = \log A - \left(\frac{E_a}{2.303R}\right)\left(\frac{1}{T}\right)$$

where $R$, $T$, $E_a$, and $A$ are the gas constant, temperature (K), apparent activation energy, and Arrhenius factor, respectively. By comparing the activation energy in the uninhibited and inhibited systems, valuable insights into the mechanism of the adsorption routes of the SP extract inhibitor could be obtained.

The slope of the straight line in Fig. 8 is utilized to calculate $E_a$ values. In comparing the $E_a$ values of the uninhibited acidic solution (15.03 kJ mol$^{-1}$) and the inhibited one (8.916 kJ mol$^{-1}$), it is evident that the chemical adsorption process is more pronounced in the former. This could be attributed to a change in the overall degradation pattern, shifting from exposed surfaces to areas that have undergone adsorption. This results in a significant decrease in activation energy at an enhanced level of the protective process. This is done by overlapping the electron density of the SP extract molecules with unfilled d-orbitals of iron to control the anodic process of a corrosion reaction and validate the chemical adsorption mechanistic pathway *via* the formation of a coordination bond. The Langmuir isotherm was used to analyze the experimental data of the adsorption process of the SP extract inhibitor on carbon steel in the 0.5 N HCl corrosive solutions under investigation. Fig. 9 presents the Langmuir adsorption model[80] shown as $C_{inh}/\theta$ *vs.* $C_{inh}$.

Thermodynamic parameters are necessary for comprehending the mitigation process's mechanistic pathway. The variable$\Delta G^0_{ads}$, representing the degree of standard free energy, can be acquired *via* the formula recorded in previous publications.[83] The $\Delta G^0_{ads}$ results are typically utilized to confirm the adsorption classification[84] between the carbon steel surface and SP extract inhibitor. The computed values for the adsorption constant ($K_{ads}$) and the standard Gibbs free energy change ($\Delta G^0_{ads}$) are 1.991 L g$^{-1}$ and −35.94 kJ mol$^{-1}$, respectively. The decent value of $K_{ads}$ indicates that the SP inhibitor molecules bind more efficiently with the carbon steel surface, providing improved protection. These findings were consistent with previous studies in the literature.[85,86] The $K_{ads}$ value showed that the adsorption of SP inhibitor molecules on the surface of carbon steel was a complicated process that involved both chemical and physical adsorption. This means that between −20 and −40 kJ mol$^{-1}$, physisorption and chemisorption occur together.[87]

### 3.3. FE-SEM investigation

The surface morphology of carbon steel was analyzed to explore the inhibitory properties of SP extract. Fig. 10 shows FE-SEM images of the carbon steel surface after being in 0.5 N HCl for 72 hours with and without 2.5 g L$^{-1}$ of SP extract inhibitor. There were deep ravines and large pits on the carbon steel surface without SP, which was significantly different from the polished surface (Fig. 10a). As shown in Fig. 10b, this indicated severe corrosion of carbon steel in a 0.5 N HCl solution.[88] However, it was clear that the carbon steel surface had a smoother shape when 2.5 g L$^{-1}$ of SP was added.[89] This differs

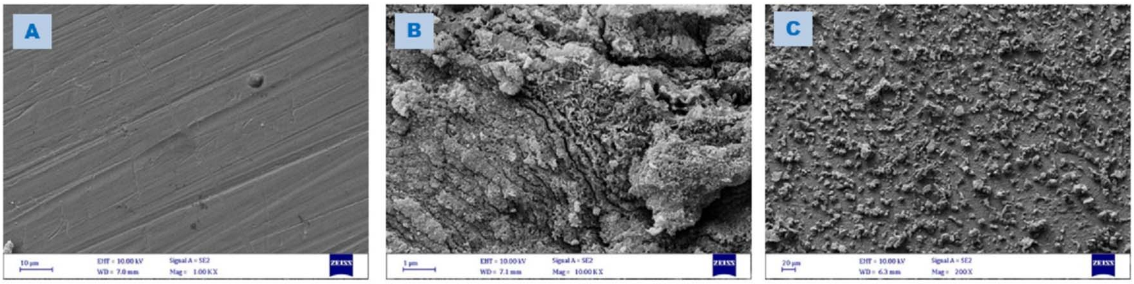

Fig. 10 SEM images of (A): polished steel, (B): steel/0.5 N HCl and (C): SP/steel/0.5 N HCl.

from the polished surface morphology; in the presence of SP extract, the inhibitor forms a dispersed aggregative layer across the entire steel surface, indicating effective adsorption. These events also showed that the inhibitor molecules adsorbed to the carbon steel's surface and formed a protective film. As seen in Fig. 10c, this blocked the corrosion that the acidic solution was causing.

## 3.4. Adsorption of SP analysis

**3.4.1 ATR-FTIR analysis.** Fig. 11 signifies the ATR-FTIR spectrum of SP inhibitor and the construction of a protective film on the carbon steel surface after immersion for 24 h in 0.5 N HCl with the optimum concentration of 2.5 g $L^{-1}$ of SP inhibitor, as shown in Fig. 11. The significant peak intensities of the SP extract were observed; the peak intensity at 3386.7 $cm^{-1}$ was attributed to phenolic (–OH) stretching vibration. The peak intensity at 3171.5 $cm^{-1}$ corresponded to (–H–C═C–H–) stretching vibration due to asymmetric stretching of alkene. Also, the peak intensity at 2962.3 $cm^{-1}$ corresponded to (–C–H) stretching vibration due to alkanes. It was also strong at 2962.3 $cm^{-1}$ for a stretching C–H $sp^3$ of hydrocarbon chains. So, it was seen to be weak at 2424.4 $cm^{-1}$ for stretching of methylene ($-CH_2-$) groups symmetrically. In addition, a peak at 2054.4 $cm^{-1}$ was the corresponding aldehyde peak due to C═ stretching vibration. Moreover, the attained peak at 1672.6 $cm^{-1}$ is behind carbonyl (C═O) stretching vibrations. Also, the strengths seen at 1596.3 $cm^{-1}$ and 1485.5 $cm^{-1}$ were due to amines' N–H bending vibrations and amides' –C–N stretching vibrations. However, the peak at 1272.5 $cm^{-1}$ was associated with ($-CH_2$) out-of-plane deformation vibration modes. Meanwhile, the peak at 1110.4 $cm^{-1}$ corresponds to a symmetric stretch of the –(C–O–C) bond. Another critical point is that the (C═C–H) bending of *trans*-disubstituted olefin groups causes the peak at 801.3 $cm^{-1}$. So, the peak at 604.8 $cm^{-1}$ is due to carbon–hydrogen bonds, which can be put into two groups: symmetric in-plane and out-of-plane deformation bending modes. It can be seen in Fig. 11 that the ATR-FTIR spectra of the protective film formed on the carbon steel surface showed all the characteristic peaks of the SP pure inhibitor, indicating that the inhibitor adsorbed on the carbon steel surface. From the obvious peaks, function groups such as C═O and NH appear on the carbon steel surface. Besides, there were small changes, and some frequencies of weak function groups were shifted significantly in the case of SP-carbon steel, as shown in Fig. 11. The above findings clearly illustrate that the

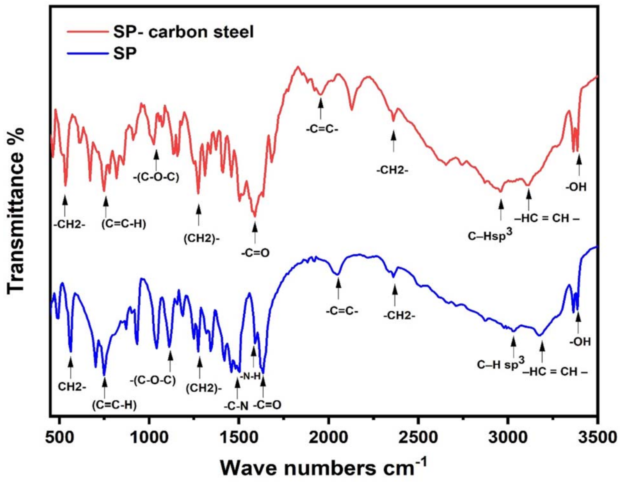

Fig. 11 ATR-FTIR spectrum of SP inhibitor on the carbon steel surface after immersion for 24 h in 0.5 N HCl with the optimum concentration of 2.5 g $L^{-1}$ of SP inhibitor.

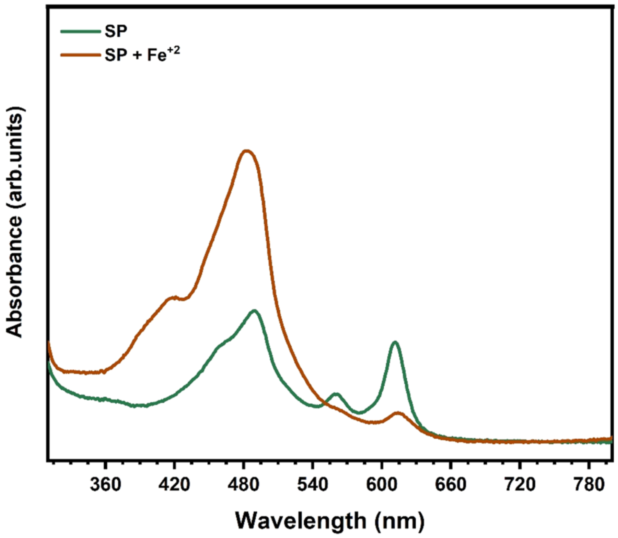

Fig. 12 UV-visible spectra of SP before and after immersion in carbon steel.

molecules of the SP extract enhanced the inhibition of corrosion by the adsorption process and hence retarded the corrosion.

**3.4.2 UV-visible investigation.** UV-visible spectroscopy observations were conducted to understand the possibility of complex formation between carbon steel and the SP inhibitor. It has been demonstrated that a change in the value of absorbance or change in the position of the absorption maximum results in a complicated configuration between two species in solution. Fig. 12 shows UV-visible spectra of SP before and after immersion in carbon steel, measuring inhibitor adsorption on the metal surface. The UV-visible spectrum of SP before metal treatment shows two peaks at 491 and 621 nm, corresponding to the π–π* transition from C═N and n–π* transition from C═O functional groups. After metal exposure, the spectrum exhibits the same absorption peaks with small modifications. The absorption peaks showed a minor hypsochromic shift. Changes in the absorption band confirm the combination of SP and $Fe^{2+}$ ions formed during the corrosion reaction.[90]

### 3.5. Computational results

**3.5.1 Optimization and frontier molecular orbital analysis (FMOs).** At first, we have optimized all five compounds which are shown in Fig. 13. According to Frontier Molecular Orbital (FMO) theory, the effectiveness of corrosion inhibitors can be predicted based on their electronic structure. The Highest Occupied Molecular Orbital (HOMO) energy level indicates the molecule's ability to donate electrons, while the Lowest Unoccupied Molecular Orbital (LUMO) energy level represents its capacity to accept electrons.[91] An ideal corrosion inhibitor should have a high HOMO energy and a low LUMO energy. A high HOMO energy means the inhibitor is more likely to donate electrons to the metal surface, forming a protective layer.[92,93] A low LUMO energy indicates that the inhibitor is less likely to accept electrons from the metal, preventing the corrosion process. Therefore, an inhibitor molecule with a large difference between its HOMO and LUMO energies is generally considered a more effective corrosion inhibitor.[94,95] The HOMO value for compounds **1–5** are computed to be −7.34 eV, −6.65 eV, −6.15 eV, −6.63 eV and −7.35 eV respectively see Fig. 14. The compound **3** has the greatest $E_{\mathrm{HOMO}}$ value compared to those of other species. The LUMO value for compounds **1–5** are computed to be −0.89 eV, −0.07 eV, −1.40 eV, −0.63 eV and −0.04 eV respectively. The compound **3** has the lowest $E_{\mathrm{LUMO}}$ value compared to those of other species. Reducing the energy gap between the HOMO and LUMO levels ($\Delta E$) is crucial for enhancing the corrosion inhibition properties of these compounds. A smaller $\Delta E$ suggests a greater propensity for electron transfer, which is a key factor in forming protective layers on the metal surface.[96,97] The energy gap ($\Delta E$) for compounds **1–5** are computed as 6.44 eV, 6.58 eV, 4.75 eV, 6.00 eV and 7.31 eV respectively. The energy gap ($\Delta E$) between the HOMO and LUMO levels of compound **3** is smaller than that of the other species. This suggests that compound **3** is more likely to be adsorbed onto the metal surface, due to its increased propensity for electron transfer.[98,99]

The FMOs research is further substantiated by the density of states (DOS) analysis shown in Fig. 15, which quantifies the number of states within a unit energy interval of the system.[100,101] The density of states (DOS) quantifies the number of states within a unit energy interval and is crucial for analyzing fragment interactions and their contributions to molecular orbitals (MOs).

The analysis of FMOs, their percentage composition, and the density of states around HOMOs and LUMOs demonstrated that differing electron-withdrawing strengths of acceptor components may substantially modify the electron density distribution on molecular orbitals. Positive and negative energy values on the density of states graph indicate bonding and antibonding orbitals, respectively. A value of 0 indicates the absence of contact between bonding orbitals. DOS computations validate the FMO results. The distribution patterns of HOMO and LUMO, as well as the energy gap between them, fluctuate based on the acceptor groups. Thus, DOS spectra can quantitatively evaluate the existence of contacts.

Additionally, these frontier molecular orbitals (FMOs) are employed to examine global reactivity descriptors and analyze the properties of the investigated compounds **1–5**.[102] This information can be used to understand the relationship between energy, structure and reactivity characteristics of complexes such as IP (Ionization Potential), EA (Electron Affinity), electronegativity ($\chi$), hardness ($\eta$), softness ($s$), and

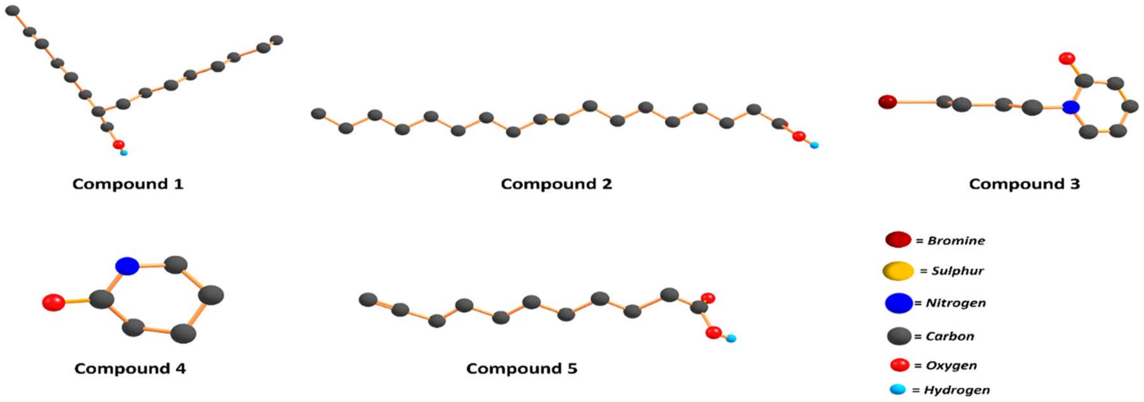

Fig. 13 Optimized structures of compounds **1–5**.

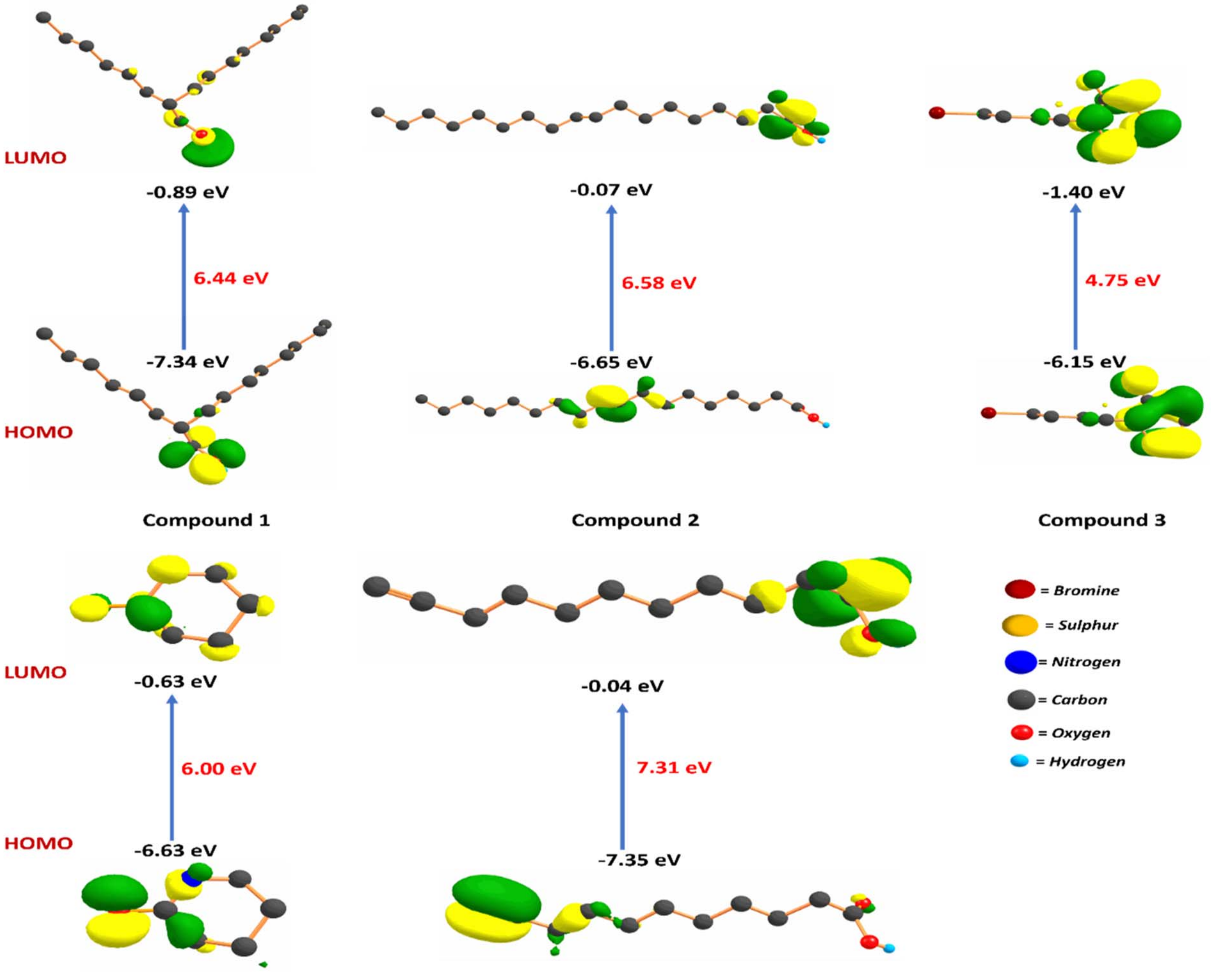

Fig. 14 Frontier molecular orbitals and energy gap of compounds **1–5**.

dipole moment ($\mu$). The global reactivity descriptors utilizing Koopman's theorem[103,104] can be described as follows,

$$\text{IP (ionization potential)} = -E_{\text{HOMO}} \tag{4}$$

$$\text{EA (electron affinity)} = -E_{\text{LUMO}} \tag{5}$$

$$\text{Hardness}\,(\eta) = \frac{(\text{IP} - \text{EA})}{2} \tag{6}$$

$$\text{Softness}\,(s) = \frac{1}{\eta} \tag{7}$$

$$\text{Electronegativity}\,(\chi) = \frac{(\text{IP} + \text{EA})}{2} \tag{8}$$

$$\Delta E_{\text{back-donation}} = \frac{-\eta}{4} \tag{9}$$

A low electronegativity ($\chi$) value often signifies the inhibitors' tendency to donate electrons to the metal surface. In contrast, inhibitor molecules with elevated electronegativity have an increased propensity to receive an electron from the steel contact, a process known as "back-donation", thereby forming a stronger connection with the metal surface.[105] Table 4 indicates that all species have elevated electronegativity, indicating their tendency to participate in back-donation and establish stronger connections with the metal contact. Moreover, softness ($s$) and hardness ($\eta$) function as metrics for the stability and reactivity of inhibitor compounds. Soft molecules have enhanced protective properties relative to hard molecules due to their efficient electron transfer to the contacting metal surface during adsorption, rendering them more effective corrosion inhibitors.[106]

As shown in Table 4, compound **3** demonstrates superior inhibitory properties attributed to its higher $\sigma$ value and lower $\eta$ value compared to the other species. Additionally, the inhibitor's ability to donate or accept electrons is evaluated by the fraction of $\Delta E_{\text{back-donation}}$. Moreover, when the $\Delta E_{\text{back-donation}}$ value is negative, it signifies that the molecule withdraws an electron from the metal surface atoms. In response, the metal atoms, now electron-deficient, tend to reclaim an electron from the molecule through back-donation. This dynamic exchange is energetically favourable and leads to a stronger interaction

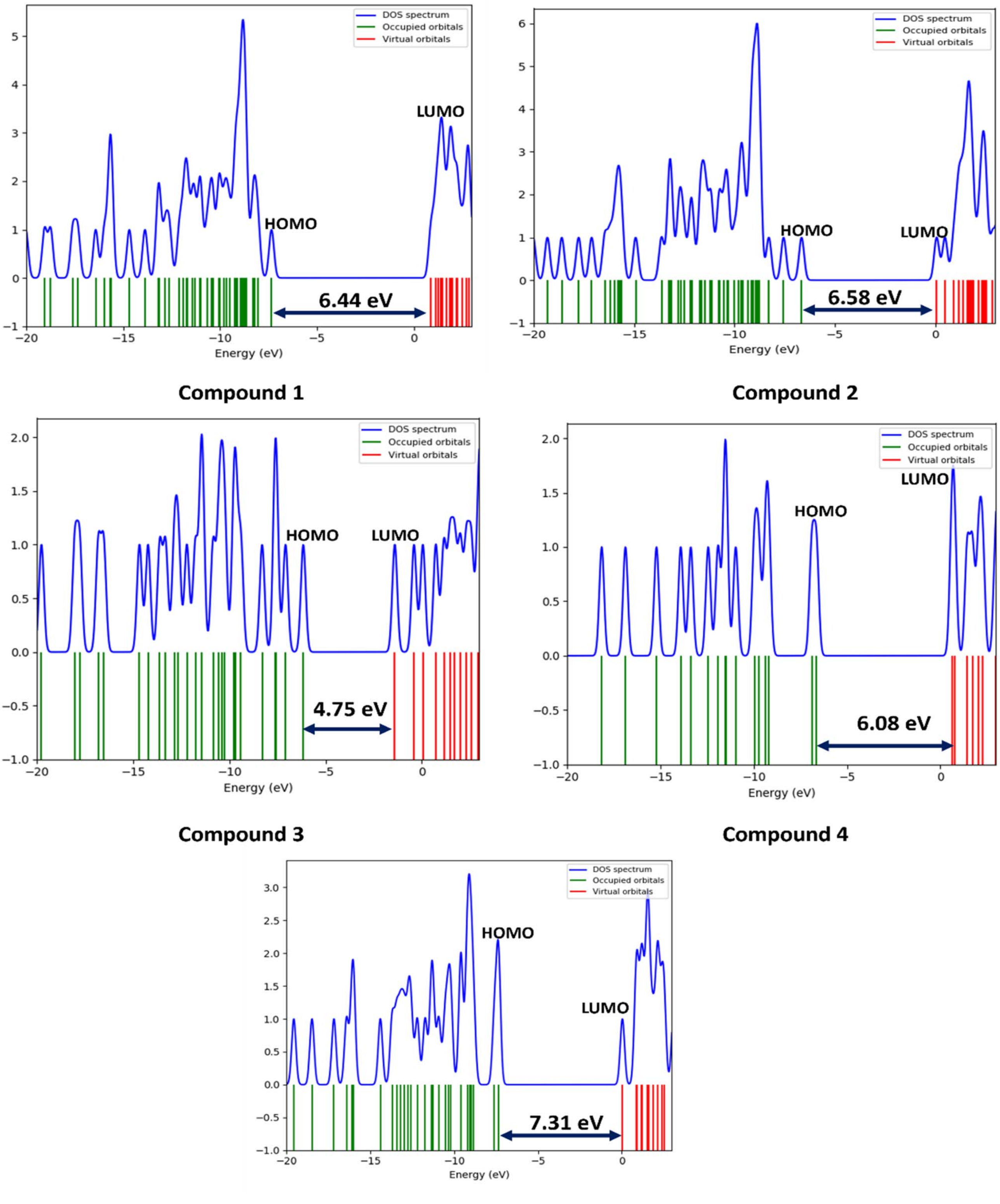

Compound 1

Compound 2

Compound 3

Compound 4

Compound 5

Fig. 15 Density of states of compounds **1–5**.

between the molecule and the metal surface.[107] As illustrated in Table 4, the $\Delta E_{\text{back-donation}}$ values for all compounds **1–5** are negative, suggesting that back-donation is a preferred mechanism for these species to establish a robust bond with the metal interface. The dipole moment serves as another critical parameter within the corrosion protection prognosis approach.

Table 4 Global descriptor parameters for compounds **1–5**

| Compounds | HOMO (eV) | LUMO (eV) | $E_g$ (eV) | $\eta$ (eV) | $\mu$ (debye) | $S$ (eV) | $\chi$ (eV) | $\Delta E_{\text{back-donation}}$ (eV) |
|---|---|---|---|---|---|---|---|---|
| **1** | −7.34 | −0.89 | 6.44 | 3.22 | 1.43 | 0.31 | −4.11 | −0.80 |
| **2** | −6.65 | −0.07 | 6.58 | 3.29 | 1.86 | 0.30 | −3.36 | −0.82 |
| **3** | −6.15 | −1.40 | 4.75 | 2.37 | 4.61 | 0.42 | −3.77 | −0.59 |
| **4** | −6.63 | −0.63 | 6.00 | 3.00 | 4.05 | 0.33 | −3.63 | −0.75 |
| **5** | −7.35 | −0.04 | 7.31 | 3.65 | 1.38 | 0.27 | −3.69 | −0.91 |

An increase in dipole moment leads to enhanced adsorption of the molecule onto the metallic surface and a corresponding increase in distortion energy.[108] Consequently, a higher dipole moment generally correlates with improved corrosion inhibition. As shown in Table 4, compound **3** exhibits a significantly higher dipole moment (4.61 debye) compared to the other compounds (compound **1**: 1.43 debye, compound **2**: 1.86 debye, compound **4**: 4.05 debye, compound **5**: 1.38 debye). The superior inhibition efficiency of the SP extract at 2.5 g $L^{-1}$ (89.56%) correlates well with the presence of compound **3** as the dominant constituent. Its favorable electronic structure including the presence of electronegative atoms (N and O) supports coordination with Fe atoms, forming a protective layer that reduces corrosion, the lowest $\Delta E$ value (indicating enhanced reactivity and adsorption tendency) that facilitates electron transfer between the inhibitor and the metal surface and the highest dipole moment (suggesting stronger interaction with the metal surface) that enhances adsorption by promoting orientation toward the charged metal surface, provides a molecular-level explanation for the observed electrochemical behavior.[109] This suggests that compound **3** has a greater affinity for adsorption on the metal surface, potentially resulting in enhanced corrosion protection.

**3.5.2 Molecular electrostatic potential (MEP).** MEP maps are crucial instruments for pinpointing reactive regions within molecules, indicating possible areas for electrophilic and nucleophilic interactions. MEP fundamentally represents the energy resulting from the interaction between a molecule's charge dispersion and a positive point charge. The color gradient on MEP maps uses red, blue, and green to denote negative, positive, and neutral areas, respectively.[110] A red area signifies a pronounced negative nucleophilic nature, rendering it vulnerable to electrophilic assault. In contrast, a dark blue area indicates an electrophilic characteristic, exhibiting a strong positive charge and susceptibility to nucleophilic assault. The yellow zone exhibits a lesser degree of negativity compared to the red region, while the light blue region displays a lesser degree of positivity than the dark blue region. The green hue signifies a virtually neutral potential in comparison to both the red and blue areas.[111–119]

Compound **1** exhibits a red colour surrounding the oxygen atom, a blue colour over the hydrogen of the hydroxyl group, and a green colour enveloping the entire decane carbon chain. Compound **2** displays a red color surrounding the oxygen atom, a blue color over the hydrogen of the hydroxyl group, and a green color encompassing the entire octadec-9-ene carbon chain. Compound **3** exhibits a red color surrounding the oxygen atom, a blue color over the hydrogen of the piperdone ring, and a green color enveloping the entire bromobutyl chain.

Compound **4** exhibits a red color surrounding the oxygen atom, a blue color over the "NH" group that is azane of the piperdone ring, and a green color enveloping the entire piperidine ring. Compound **5** displays a red color surrounding the oxygen atom, a blue color over the hydrogen of the hydroxyl group, and a green color encompassing the entire tetradecane chain see Fig. 16. The electronegative potential values for compound **1**, compound **2**, compound **3**, compound **4** and compound **5** are $-4.972 \times 10^{-2}$, $-5.312 \times 10^{-2}$, $-5.880 \times 10^{-2}$, $-6.490 \times 10^{-2}$ and $-5.427 \times 10^{-2}$ respectively. MEP maps indicate that compound **4** possesses the highest electronegative potential compared to the other species.

### 3.6. Inhibition mechanism of SP extract

Based on experimental observations (EIS, ATR-FTIR, FE-SEM/EDX) and theoretical calculations (DFT), we propose the following inhibition mechanism for SP extract on carbon steel in 0.5 M HCl solution:

In the absence of the inhibitor, corrosive species such as $H^+$, $Cl^-$, and $H_2O$ can easily reach the steel surface, leading to severe corrosion.[120] When Sp extract is introduced into the medium, it contains several electron-rich compounds, including 2-piperidinone, *N*-[4-bromo-*n*-butyl], 9-octadecenoic acid and tetradecyl undec-10-ynoate. These compounds possess heteroatoms (N, O) and conjugated systems, enabling them to donate electron pairs to vacant d-orbitals of Fe atoms on the carbon steel surface. This leads to the formation of: Fe–N and Fe–O coordination bonds, confirmed by ATR-FTIR analysis showing characteristic peaks corresponding to these bonds after immersion in SP-containing solution. A protective adsorbed layer that physically blocks aggressive ions ($H^+$, $Cl^-$) from reaching the metal surface.[121] From PDP results: The $E_{\text{corr}}$ shift was less than ±85 mV, indicating mixed-type inhibition, where both anodic dissolution and cathodic hydrogen evolution are suppressed. DFT calculations further support this behavior by showing that key compounds (especially compound **3**) exhibit strong reactivity toward both oxidation and reduction reactions. The variation in $R_{\text{ct}}$ and $\text{CPE}_{\text{dl}}$ with SP concentration fits well with the Langmuir isotherm, suggesting: monolayer adsorption of inhibitor molecules on the steel surface and no lateral interactions between adsorbed molecules. Maximum surface coverage at 2.5 g $L^{-1}$, consistent with the highest inhibition efficiency observed. FE-SEM/EDX analysis showed a smooth, uniform

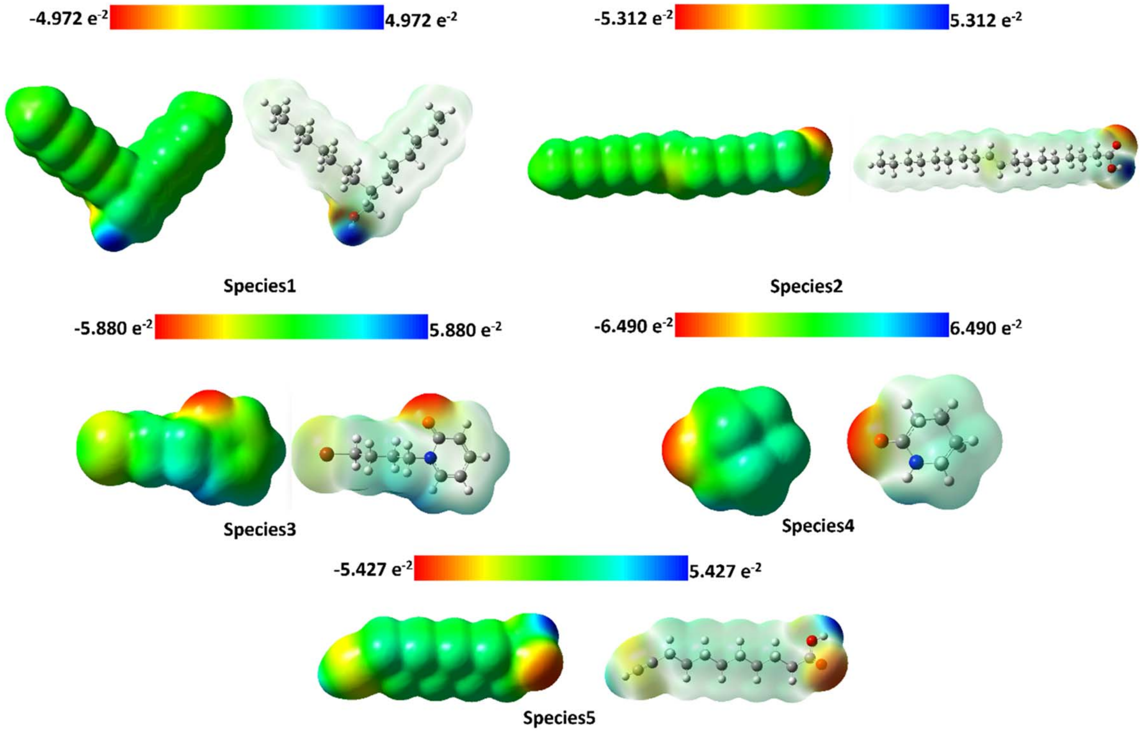

Fig. 16 MEP maps of compounds **1–5**.

Table 5 Comparison of the inhibition efficiencies (IE %) of SP extract with other extracts from literature

| Extract name | Extraction method | Plant part used | Medium | Substrate | Concentration | IE % | Ref. |
|---|---|---|---|---|---|---|---|
| *Dactyloctenium aegyptium* extract | — | Whole plant | 0.5 M HCl | Carbon steel | 800 ppm | PDP: 76.5<br>EIS: 70.6 | 122 |
| *Kopsia teoi* extracts (KTDAE) | Maceration | Aerial parts | 0.5 M HCl | Mild steel | 500 ppm | PDP: 77.84<br>EIS: 87.04 | 123 |
| Heat-assisted extracted *Melilotus officinalis* (HAE) | Heat-assisted extraction | Leaves | 0.5 M HCl | Carbon steel | 800 ppm | PDP: 82.0<br>EIS: 82.3 | 124 |
| *Cleome arabica* L. extract | Soaking | Whole plant | 0.5 M HCl | AISI 1045 carbon steel | 1.0 g $L^{-1}$ | PDP: 87.89<br>EIS: 77.8 | 125 |
| Safflower extract (SP) | Soxhlet extraction | Whole plant (flower/leaves) | 0.5 M HCl | Carbon steel | 2.5 g $L^{-1}$ | PDP: 89.56<br>EFM: 84.07<br>EIS: 84.65 | This study |

layer formed on the steel surface in the presence of SP extract. EDX spectra confirmed the presence of N and O from the extract on the inhibited surface, reinforcing the adsorption mechanism. DFT results highlighted compound **3** (1-(4-bromobutyl) piperidin-2-one) as the most active component due to: highest HOMO energy → strong electron donating capability, lowest LUMO energy → high electron accepting tendency, smallest energy gap ($\Delta E$) → enhanced reactivity and High dipole moment → better orientation towards the metal surface. These properties align with the observed strong adsorption and high inhibition efficiency.

Table 5 presents data on plant extracts, as reported in the literature, along with their inhibition efficiencies.[122–125] The inhibition efficiency of SP extract against carbon steel alloy corrosion was comparable and exceeded that of several extracts in literature. The inclusion of 'method of extraction' and 'plant part used' highlights the importance of preparation techniques and source material in determining the efficacy of plant-based corrosion inhibitors. For instance, the Soxhlet extraction method used in this study ensures a higher yield of active compounds compared to simple maceration or soaking methods, potentially contributing to the superior inhibition efficiency observed for SP extract. In this study, SP extract achieved higher efficiency (PDP = 89.56%) than previously reported extracts (76.5%, 77.84%, 82.0%, and 87.89%). These results indicate that this research builds logically on prior studies of plant extracts as green inhibitors.

## 4. Conclusion

The findings of this study demonstrate that safflower plant (SP) extract is a highly effective green corrosion inhibitor for carbon steel in acidic environments. The extract significantly reduces the corrosion rate and enhances inhibition efficiency, particularly at higher concentrations (up to 2.5 g $L^{-1}$). The mechanism of inhibition is attributed to both physical and chemical adsorption, as supported by experimental and computational data. The Langmuir adsorption model successfully described the inhibitor's adsorption behavior. Theoretical studies using density functional theory (DFT) further elucidated the interaction between key active compounds in the SP extract and the metal surface, confirming their role in inhibiting corrosion. Computational modeling and analysis of the five studied complexes (compounds **1–5**) reveal significant insights into their corrosion inhibition potential. Among them, compound **3** stands out as the most effective inhibitor, demonstrated by its highest HOMO energy, lowest LUMO energy, and smallest energy gap ($\Delta E$), which indicate strong electron-donating capability and superior adsorption onto metal surfaces. Density of States (DOS) analysis and global reactivity descriptors, including ionization potential, electron affinity, and dipole moment, further confirm compound **3**'s superior inhibitory properties. While Molecular Electrostatic Potential (MEP) mapping highlights compound **4**'s highest electronegative potential, compound **3**'s optimal electronic structure and reactivity make it the most promising candidate for corrosion protection. The SP extract provides a promising, eco-friendly alternative to conventional synthetic inhibitors, making it suitable for applications in industries where acidic solutions are used.

## Data availability

The datasets generated during and/or analyzed during the current study are available from the author on reasonable request.

## Conflicts of interest

The authors declare that they have no known competing financial interests or personal relationships that could have appeared to influence the work reported in this paper.

## Acknowledgements

The authors are thankful to the Deanship of Graduate Studies and Scientific Research at University of Bisha for supporting this work through the Fast-Track Research Support Program.

## References

1 Q. A. Yousif, Z. Fadel, A. M. Abuelela, E. H. Alosaimi, S. Melhi and M. A. Bedair, *RSC Adv.*, 2023, **13**, 13094–13119.
2 K. Sayin, H. Jafari and F. Mohsenifar, *J. Taiwan Inst. Chem. Eng.*, 2016, **68**, 431–439.
3 A. A. Bahraq, I. B. Obot, M. A. Al-Osta and M. Ibrahim, *Constr. Build. Mater.*, 2024, **412**, 134808.
4 M. Baladi, Q. A. Yousif, M. Valian and M. Salavati-Niasari, *J. Alloys Compd.*, 2022, **896**, 163032.
5 S. Abd El Wanees, M. G. A. Saleh, M. I. Alahmdi, N. H. Elsayed, M. M. Aljohani, M. Abdelfattah, K. A. Soliman, M. Lotfy Alalati and S. S. Elyan, *Mater. Chem. Phys.*, 2024, **311**, 128484.
6 H. Jafari, F. Mohsenifar and K. Sayin, *J. Taiwan Inst. Chem. Eng.*, 2016, **64**, 314–324.
7 Z. Fadel and Q. A. Yousif, *J. Phys.:Conf. Ser.*, 2020, **1664**, 012093.
8 M. Gab-Allah, M. Bedair, A. Elged, S. Soliman, E. Badr and M. Bakr, *Egypt. J. Chem.*, 2023, **66**, 2013–2031.
9 B. Yan, J. Lv, S. Zhou, Z. Wu, X. Liu, B. Li, Q. Gao, W. Wu and G. Chen, *Biomass Bioenergy*, 2024, **184**, 107198.
10 H. Jafari, K. Akbarzade and I. Danaee, *Arabian J. Chem.*, 2019, **12**, 1387–1394.
11 M. N. Majeed and Q. A. Yousif, *J. Nanostruct.*, 2022, **12**, 616–624.
12 A. Fahmy, M. El Sabbagh, M. Bedair, A. Gangan, M. El-Sabbah, S. M. El-Bahy and J. F. Friedrich, *J. Adhes. Sci. Technol.*, 2021, **35**, 1734–1751.
13 Z. Song, L. Liu, M. Z. Guo, H. Cai, Q. Liu, S. Donkor and H. Zhao, *Case Stud. Constr. Mater.*, 2024, **20**, e02992.
14 H. Jafari, E. Ameri, M. Rezaeivala, A. Berisha and J. Halili, *J. Phys. Chem. Solids*, 2022, **164**, 110645.
15 P. D. Desai, C. B. Pawar, M. S. Avhad and A. P. More, *Vietnam J. Chem.*, 2023, **61**, 15–42.
16 S. Melhi, M. A. Bedair, E. H. Alosaimi, A. A. O. Younes, W. H. El-Shwiniy and A. M. Abuelela, *RSC Adv.*, 2022, **12**, 32488–32507.
17 A. Royani, M. Hanafi, R. Haldhar and A. Manaf, *J. Engine Res.*, 2024, **12**(3), 321–327.
18 Q. A. Yousif, A. Abdel Nazeer, Z. Fadel, L. A. Al-Hajji and K. Shalabi, *ACS Omega*, 2024, **9**, 14153–14173.
19 E. S. Gad, M. A. Abbas, M. A. Bedair, O. E. El-Azabawy and S. M. Mukhtar, *Sci. Rep.*, 2023, **13**, 1–27.
20 B. Benzidia, M. Barbouchi, M. Rehioui, H. Hammouch, H. Erramli and N. Hajjaji, *J. King Saud Univ., Sci.*, 2023, **35**, 102986.
21 H. Jafari, I. Danaee, H. Eskandari and M. RashvandAvei, *J. Mater. Sci. Technol.*, 2014, **30**, 239–252.
22 T. N. Tran, T. T. Tran, D. S. Jo, P. S. N. Dong, V. K. Nguyen, T. L. Huynh and N. Nguyen Dang, *J. Ind. Eng. Chem.*, 2024, **135**, 175–187.
23 Q. A. Yousif, *IOP Conf. Ser.: Earth Environ. Sci.*, 2021, **790**, 012072.
24 Q. A. Yousif, M. A. Bedair, Z. Fadel, F. Al-Odail and A. M. Abuelela, *Inorg. Chem. Commun.*, 2024, **164**, 112454.
25 H. Ferkous, A. Sedik, A. Delimi, R. Redjemia, K. Abdesalem, C. Boulechfar, A. Abdennouri, A. Madaci, M. Berredjem, A. Boublia, M. Sajid Ali, B. H. Jeon, K. Kumar Yadav and Y. Benguerba, *J. Mol. Liq.*, 2024, **394**, 123781.
26 Z. Fadel and Q. A. Yousif, *IOP Conf. Ser.: Earth Environ. Sci.*, 2021, **790**, 012074.
27 B. Weng, M. Y. Qi, C. Han, Z. R. Tang and Y. J. Xu, *ACS Catal.*, 2019, **9**, 4642–4687.
28 R. Lachhab, M. Galai, A. Ech-chebab, R. A. Belakhmima, M. E. Touhami and I. Mansouri, *Ceram. Int.*, 2024, **50**, 4282–4295.

29 B. Benzidia, M. Barbouchi, R. Hsissou, M. Zouarhi, H. Erramli and N. Hajjaji, *Curr. Res. Green Sustainable Chem.*, 2022, **5**, 100299.
30 N. Alipanah, A. Dehghani, A. Hossein Jafari Mofidabadi, M. Salamati and B. Ramezanzadeh, *J. Mol. Liq.*, 2024, **393**, 123554.
31 Y. Di, X. Li, Z. Chen, X. Yin, Y. Chen, Y. Liu and W. Yang, *J. Mol. Struct.*, 2022, **1268**, 133737.
32 H. Mahmoudi-Moghaddam, M. Amiri, H. Akbari Javar, Q. A. Yousif and M. Salavati-Niasari, *Arabian J. Chem.*, 2022, **15**, 103988.
33 Y. Meng, S. Li and Z. Zhang, *Heliyon*, 2024, **10**, e24688.
34 J. xin Song, H. jie Zhang, M. hong Niu, Y. zhu Guo and H. ming Li, *Ind. Crops Prod.*, 2024, **214**, 118443.
35 M. Valian, F. Soofivand, A. Khoobi, Q. A. Yousif and M. Salavati-Niasari, *Arabian J. Chem.*, 2022, **16**, 104401.
36 J. Wang, Y. Cao, J. Xue, X. Zhang, Y. Liang, K. Chen, C. Huang and D. Zheng, *Corros. Sci.*, 2024, **231**, 111994.
37 M. H. Shahini, M. Ramezanzadeh and B. Ramezanzadeh, *Colloids Surf., A*, 2022, **634**, 127990.
38 A. Kumar, J. Kumar and Nishtha, *Mater. Today: Proc.*, 2022, **64**, 141–146.
39 D. S. Chauhan, M. A. Quraishi, A. A. Sorour and C. Verma, *J. Pet. Sci. Eng.*, 2022, **215**, 110695.
40 A. M. Abuelela, J. Kaur, A. Saxena, M. A. Bedair, D. K. Verma and E. Berdimurodov, *Sci. Rep.*, 2023, **13**, 19367.
41 K. Zakaria, M. A. Abbas and M. A. Bedair, *J. Mol. Liq.*, 2022, **352**, 118689.
42 B. Liao, Z. Luo, S. Wan and L. Chen, *J. Ind. Eng. Chem.*, 2023, **117**, 238–246.
43 Q. A. Yousif, Z. Fadel, A. M. Abuelela, E. H. Alosaimi, S. Melhi and M. A. Bedair, *RSC Adv.*, 2023, **13**, 13094–13119.
44 M. Galai, K. Dahmani, O. Kharbouch, M. Rbaa, N. Alzeqri, L. Guo, A. A. AlObaid, A. Hmada, N. Dkhireche, E. Ech-chihbi, M. Ouakki, M. E. Touhami and I. Warad, *J. Phys. Chem. Solids*, 2024, **184**, 111681.
45 H. Jafari and E. Ameri, *Anti-Corros. Methods Mater.*, 2024, **71**, 632–639.
46 R. Aslam, G. Serdaroglu, S. Zehra, D. Kumar Verma, J. Aslam, L. Guo, C. Verma, E. E. Ebenso and M. A. Quraishi, *J. Mol. Liq.*, 2022, **348**, 118373.
47 H. Ahchouch, M. El house, A. H. Al-Moubaraki, E. A. Noor, A. Hadfi, A. Driouiche, L. Bammou, M. Belkhaouda, R. Salghi, M. Chafiq, A. Chaouiki and Y. G. Ko, *Arabian J. Chem.*, 2024, **17**, 105593.
48 O. Ninich, A. Et-tahir, K. Kettani, M. Ghanmi, J. Aoujdad, S. El Antry, M. Ouajdi and B. Satrani, *J. Ethnopharmacol.*, 2022, **285**, 114889.
49 M. Bedair, M. Metwally, S. Soliman, A. Al-Sabagh, A. Salem and T. Mohamed, *Al-Azhar Bull. Sci.*, 2015, **26**, 1–14.
50 R. Haldhar, S.-C. Kim, D. Prasad, M. A. A. Bedair, I. Bahadur, S. Kaya, O. Dagdag and L. Guo, *J. Mol. Struct.*, 2021, **1242**, 130822.
51 A. E. A. S. Fouda, A. A. Nazeer and A. Saber, *J. Korean Chem. Soc.*, 2014, **58**, 160–168.
52 M. Nasibi, D. Zaarei, G. Rashed and E. Ghasemi, *Chem. Eng. Commun.*, 2013, **2003**, 367–378.
53 M. N. Majeed, Q. A. Yousif and M. A. Bedair, *ACS Omega*, 2022, **7**, 29850–29857.
54 A. Gangan, M. ElSabbagh, M. A. Bedair, H. M. Ahmed, M. El-Sabbah, S. M. El-Bahy and A. Fahmy, *Arabian J. Chem.*, 2021, **14**, 103391.
55 M. A. Bedair, A. M. Abuelela, S. Melhi, Q. A. Yousif, V. V. Chaban and E. H. Alosaimi, *Mater. Chem. Phys.*, 2024, **312**, 128644.
56 Semichem Inc., *Semichem Inc:GaussView 6*, 2016.
57 M. J. Frisch, G. W. Trucks, H. B. Schlegel, G. E. Scuseria, M. A. Robb, J. R. Cheeseman, G. Scalmani, V. Barone, G. A. Petersson, H. Nakatsuji, X. Li, M. Caricato, A. V Marenich, J. Bloino, B. G. Janesko, R. Gomperts, B. Mennucci, H. P. Hratchian, J. V. Ortiz, A. F. Izmaylov, J. L. Sonnenberg, D. Williams-Young, F. Ding, F. Lipparini, F. Egidi, J. Goings, B. Peng, A. Petrone, T. Henderson, D. Ranasinghe, V. G. Zakrzewski, J. Gao, N. Rega, G. Zheng, W. Liang, M. Hada, M. Ehara, K. Toyota, R. Fukuda, J. Hasegawa, M. Ishida, T. Nakajima, Y. Honda, O. Kitao, H. Nakai, T. Vreven, K. Throssell, J. A. Montgomery Jr, J. E. Peralta, F. Ogliaro, M. J. Bearpark, J. J. Heyd, E. N. Brothers, K. N. Kudin, V. N. Staroverov, T. A. Keith, R. Kobayashi, J. Normand, K. Raghavachari, A. P. Rendell, J. C. Burant, S. S. Iyengar, J. Tomasi, M. Cossi, J. M. Millam, M. Klene, C. Adamo, R. Cammi, J. W. Ochterski, R. L. Martin, K. Morokuma, O. Farkas, J. B. Foresman and D. J. Fox, 2016.
58 C. Lee, W. Yang and R. G. Parr, *Phys. Rev. B: Condens. Matter Mater. Phys.*, 1988, **37**, 785–789.
59 A. D. Becke, *J. Chem. Phys.*, 1993, **98**, 5648–5652.
60 M. J. Frisch, J. A. Pople and J. S. Binkley, *J. Chem. Phys.*, 1984, **80**, 3265–3269.
61 A.-R. A. Allouche, *J. Comput. Chem.*, 2011, **32**, 174–182.
62 M. A. Bedair, A. M. Abuelela, W. M. Zoghaib and T. A. Mohamed, *J. Mol. Struct.*, 2021, **1244**, 130927.
63 F. Bertin, G. R. Joshi, J. Kittel, C. Sagnard, F. Ropital, M. Martinez, C. Bosch and K. Wolski, *Corros. Sci.*, 2024, **227**, 111778.
64 M. A. Al-Masoud, M. M. Khalaf, I. M. A. Mohamed, K. Shalabi and H. M. Abd El-Lateef, *J. Ind. Eng. Chem.*, 2022, **112**, 398–422.
65 T. K. Sarkar, M. Yadav and I. B. Obot, *Chem. Eng. J.*, 2022, **431**, 133481.
66 H. Yan, S. Dai, P. Liu and Y. Zhu, *Corros. Sci.*, 2024, **227**, 111750.
67 M. A. Bedair, Q. A. Yousif, Z. Fadel, S. Melhi, F. A. Al-Odail and A. M. Abuelela, *J. Mol. Struct.*, 2025, **1328**, 141282.
68 M. A. Bedair, *Results Surf. Interfaces*, 2025, **19**, 100511.
69 A. M. Ashmawy, R. Said, I. A. Naguib, B. Yao and M. A. Bedair, *ACS Omega*, 2022, **7**, 17849–17860.
70 K. Rasheeda, N. P. Swathi, V. D. P. Alva, S. Samshuddin, T. A. Aljohani, I. Baig, F. Y. Alomari and A. H. Alamri, *S. Afr. J. Chem. Eng.*, 2024, **48**, 80–94.
71 N. A. Odewunmi, M. A. J. Mazumder and S. A. Ali, *J. Mol. Liq.*, 2022, **360**, 119431.

72 M. A. Bedair, H. M. Elaryian, A. H. Bedair, R. M. Aboushahba, A. El-Aziz and S. Fouda, *Inorg. Chem. Commun.*, 2023, **148**, 110304.

73 M. A. Abbas, E. I. Arafa, M. A. Bedair, A. S. Ismail, O. E. El-Azabawy, S. A. Baker and H. I. Al-Shafey, *Arabian J. Sci. Eng.*, 2023, **48**, 7463–7484.

74 M. A. Bedair, *Inorg. Chem. Commun.*, 2024, **167**, 112693.

75 H. M. Elaryian, M. A. Bedair, A. H. Bedair, R. M. Aboushahba and A. E.-A. S. Fouda, *RSC Adv.*, 2022, **12**, 29350–29374.

76 M. A. Bedair, E. H. Alosaimi and S. Melhi, *J. Adhes. Sci. Technol.*, 2021, **37**, 1–31.

77 H. Zhu, Y. Huo, W. Wang, X. He, S. Fang and Y. Zhang, *Process Saf. Environ. Prot.*, 2021, **148**, 624–635.

78 M. A. Bedair, S. A. Soliman and M. S. Metwally, *J. Ind. Eng. Chem.*, 2016, **41**, 10–22.

79 R. Kellal, D. Benmessaoud Left, Z. S. Safi, A. Thoume, N. A. Wazzan, O. S. AL-Qurashi and M. Zertoubi, *Mater. Chem. Phys.*, 2024, **314**, 128846.

80 R. Lei, S. Deng, Y. Qiang, D. Xu, G. Du, D. Shao and X. Li, *Colloids Surf., A*, 2024, **687**, 133358.

81 B. lan Lin, X. xin Zhou, T. hu Duan, C. Zhao, J. hao Zhu and Y. ye Xu, *Arabian J. Chem.*, 2024, **17**(1), 105410.

82 L. Cui, W. Kang, H. You, J. Cheng and Z. Li, *J. Bio-Tribo. Corros.*, 2021, **7**, 1–14.

83 T. Nesane, N. E. Madala, M. M. Kabanda, L. C. Murulana and I. Bahadur, *Colloids Surf., A*, 2023, **667**, 131405.

84 S. Lamghafri, W. Daoudi, A. El Aatiaoui, O. Dagdag, H. Kim, A. Berisha, W. B. W. Nik, A. J. Obaidullah, K. K. Yadav, A. Zarrouk and A. Lamhamdi, *J. Mol. Struct.*, 2024, **1306**, 137924.

85 B. Tamilselvi, D. S. Bhuvaneshwari, S. Padmavathy and P. B. Raja, *J. Mol. Liq.*, 2022, **359**, 119359.

86 M. A. Abbas and M. A. Bedair, *Z. Phys. Chem.*, 2019, **233**, 225–254.

87 S. S. Alarfaji, I. H. Ali, M. Z. Bani-Fwaz and M. A. Bedair, *Molecules*, 2021, **26**, 3183.

88 M. A. Abbas, E. I. Arafa, E. S. Gad, M. A. Bedair, O. E. El-Azabawy and H. I. Al-Shafey, *Inorg. Chem. Commun.*, 2022, **143**, 109758.

89 M. A. Abbas, M. A. Bedair, O. E. El-Azabawy, E. S. Gad, M. A. Abbas, M. A. Bedair, O. E. El-Azabawy and E. S. Gad, *ACS Omega*, 2021, **6**, 15089–15102.

90 H. M. Elaryian, M. A. Bedair, A. H. Bedair, R. M. Aboushahba and A. E.-A. S. Fouda, *J. Mol. Liq.*, 2022, **346**, 118310.

91 M. A. Gebril, M. A. Bedair, S. A. Soliman, M. F. Bakr and M. B. I. Mohamed, *J. Mol. Liq.*, 2022, **349**, 118445.

92 A. Kokalj, *Corros. Sci.*, 2021, **180**, 109016.

93 M. A. Deyab, Q. Mohsen and O. A. A. El-Shamy, *Colloids Surf., A*, 2024, **702**, 135024.

94 I. Lukovits, E. Kálmán and F. Zucchi, *Corrosion*, 2001, **57**, 3–8.

95 M. A. Bedair, H. M. Elaryian, E. S. Gad, M. Alshareef, A. H. Bedair, R. M. Aboushahba and A. S. Fouda, *RSC Adv.*, 2023, **13**, 478–498.

96 H. M. Abd El-Lateef, K. Shalabi and A. H. Tantawy, *New J. Chem.*, 2020, **44**, 17791–17814.

97 M. Goyal, H. Vashist, S. Kumar, I. Bahadur, F. Benhiba and A. Zarrouk, *J. Mol. Liq.*, 2020, **315**, 113705.

98 A. Dehghani, A. H. Mostafatabar, G. Bahlakeh and B. Ramezanzadeh, *J. Mol. Liq.*, 2020, **316**, 113914.

99 M. A. Bedair, A. M. Abuelela, M. Alshareef, M. Owda and E. M. Eliwa, *RSC Adv.*, 2023, **13**, 186–211.

100 S. S. Malhotra, M. Kumar, M. K. Gupta and A. Ansari, *Mater. Today Commun.*, 2024, **39**, 109208.

101 S. S. Malhotra, M. Ahmed, M. Kumar, M. A. Amin, S. M. El-Bahy, Z. M. El-Bahy, R. K. Mohapatra and A. Ansari, *Mater. Today Commun.*, 2024, **41**, 110182.

102 M. A. Bedair, S. A. Soliman, M. A. Hegazy, I. B. Obot and A. S. Ahmed, *J. Adhes. Sci. Technol.*, 2019, **33**, 1139–1168.

103 M. Govindarajan, M. Karabacak, S. Periandy and D. Tanuja, *Spectrochim. Acta, Part A*, 2012, **97**, 231–245.

104 A. M. Abuelela, M. A. Bedair, E. S. Gad, Y. F. El-Aryan, W. A. A. Arafa, A. K. Mourad, H. Nady and S. Eid, *Sci. Rep.*, 2024, **14**, 13310.

105 E. A. Badr, M. A. Bedair and S. M. Shaban, *Mater. Chem. Phys.*, 2018, **219**, 444–460.

106 M. K. Awad, M. S. Metwally, S. A. Soliman, A. A. El-Zomrawy and M. A. bedair, *J. Ind. Eng. Chem.*, 2014, **20**, 796–808.

107 M. A. Bedair, M. M. B. El-Sabbah, A. S. Fouda and H. M. Elaryian, *Corros. Sci.*, 2017, **128**, 54–72.

108 A. M. Abuelela, M. A. Bedair, W. M. Zoghaib, L. D. Wilson and T. A. Mohamed, *J. Mol. Struct.*, 2021, **1230**, 129647.

109 M. A. Bedair, *J. Mol. Liq.*, 2016, **219**, 128–141.

110 M. A. A. Bedair, S. A. A. Soliman, M. F. Bakr, E. S. S. Gad, H. Lgaz, I.-M. M. Chung, M. Salama and F. Z. Alqahtany, *J. Mol. Liq.*, 2020, **317**, 114015.

111 M. Kumar, A. K. Talakkal, R. K. Mohapatra and A. Ansari, *J. Mol. Model.*, 2023, **29**, 336.

112 M. Ahmed, M. K. Gupta and A. Ansari, *J. Mol. Model.*, 2023, **29**, 358.

113 O. Yadav, M. Ansari and A. Ansari, *Spectrochim. Acta, Part A*, 2022, **278**, 121331.

114 M. Kumar, M. Ansari and A. Ansari, *Spectrochim. Acta, Part A*, 2023, **284**, 121774.

115 R. K. Mohapatra, M. Azam, P. K. Mohapatra, A. K. Sarangi, M. Abdalla, L. Perekhoda, O. Yadav, S. I. Al-Resayes, K. Jong-Doo, K. Dhama, A. Ansari, V. Seidel, S. Verma and M. K. Raval, *J. King Saud Univ., Sci.*, 2022, **34**, 102086.

116 Monika and A. Ansari, *Struct. Chem.*, 2023, **34**, 825–835.

117 O. Yadav, M. Kumar, H. Mittal, K. Yadav, V. Seidel and A. Ansari, *Front. Pharmacol.*, 2022, **13**, 982484.

118 S. Raheem, T. Jan, A. Qayum, O. Yadav, M. Mustafa, A. Ansari, G. Mustafa Peerzada, S. K. Singh and M. Ahmad Rizvi, *Polyhedron*, 2023, **244**, 116597.

119 M. Kumar, M. K. Gupta, M. Ansari and A. Ansari, *Phys. Chem. Chem. Phys.*, 2024, **26**, 4349–4362.

120 H. Jafari, F. Mohsenifar and K. Sayin, *Iran. J. Chem. Chem. Eng.*, 2018, **37**, 85–103.

121 H. Jafari and K. Sayin, *J. Taiwan Inst. Chem. Eng.*, 2015, **56**, 181–190.

122 Raghvi, A. Saxena, J. Kaur, E. Berdimurodov and D. K. Verma, *J. Indian Chem. Soc.*, 2024, **101**(10), 101317.

123 M. T. Muhammad, M. H. Hussin, M. H. Abu Bakar, T. S. Hamidon, S. S. Azahar, K. Awang, M. Litaudon and M. N. Azmi, *Mater. Chem. Phys.*, 2024, **322**, 129584.

124 M. Iranpour, A. Babaei and M. Bagherzadeh, *Clean Chem. Eng.*, 2025, 100149.

125 I. Ait Bouabdallah, F. Adjal, A. Zaabar, A. Benchikh, D. Guerniche, C. Ait Ramdane-Terbouche, A. P. Piedade, M. Z. Ibrahim, N. Nasrallah and A. Abdi, *RSC Adv.*, 2024, **14**, 36423–36436.